The use of rotational invariants for the interpretation of marine CSEM data with a case study from the North Alex mud volcano, West Nile Delta

Sebastian Hölz,[1] Andrei Swidinsky,[2] Malte Sommer,[1] Marion Jegen[1] and Jörg Bialas[1]

[1]*Department for Geodynamics, GEOMAR Helmholtz Centre for Ocean Research Kiel, D-24148 Kiel, Germany. E-mail: shoelz@geomar.de*
[2]*Department of Geophysics, Colorado School of Mines, Golden, CO 80401, USA*

SUMMARY

Submarine mud volcanos at the seafloor are surface expressions of fluid flow systems within the seafloor. Since the electrical resistivity of the seafloor is mainly determined by the amount and characteristics of fluids contained within the sediment's pore space, electromagnetic methods offer a promising approach to gain insight into a mud volcano's internal resistivity structure. To investigate this structure, we conducted a controlled source electromagnetic experiment, which was novel in the sense that the source was deployed and operated with a remotely operated vehicle, which allowed for a flexible placement of the transmitter dipole with two polarization directions at each transmitter location. For the interpretation of the experiment, we have adapted the concept of rotational invariants from land-based electromagnetics to the marine case by considering the source normalized tensor of horizontal electric field components. We analyse the sensitivity of these rotational invariants in terms of 1-D models and measurement geometries and associated measurement errors, which resemble the experiment at the mud volcano. The analysis shows that any combination of rotational invariants has an improved parameter resolution as compared to the sensitivity of the pure radial or azimuthal component alone. For the data set, which was acquired at the 'North Alex' mud volcano, we interpret rotational invariants in terms of 1-D inversions on a common midpoint grid. The resulting resistivity models show a general increase of resistivities with depth. The most prominent feature in the stitched 1-D sections is a lens-shaped interface, which can similarly be found in a section from seismic reflection data. Beneath this interface bulk resistivities frequently fall in a range between 2.0 and 2.5 Ωm towards the maximum penetration depths. We interpret the lens-shaped interface as the surface of a collapse structure, which was formed at the end of a phase of activity of an older mud volcano generation and subsequently refilled with new mud volcano sediments during a later stage of activity. Increased resistivities at depth cannot be explained by compaction alone, but instead require a combination of compaction and increased cementation of the older sediments, possibly in connection to trapped, cooled down mud volcano fluids, which have a depleted chlorinity. At shallow depths ($\leq$50 m) bulk resistivities generally decrease and for locations around the mud volcano's centre 1-D models show bulk resistivities in a range between 0.5 and 0.7 Ωm, which we interpret in terms of gas saturation levels by means of Archie's Law. After a detailed analysis of the material parameters contained in Archie's Law we derive saturation levels between 0 and 25 per cent, which is in accordance with observations of active degassing and a reflector with negative polarity in the seismics section just beneath the seafloor, which is indicative of free gas.

Key words: Numerical approximations and analysis; Electrical properties; Marine electromagnetics; Gas and hydrate systems; Hydrothermal systems; Permeability and porosity.

INTRODUCTION

Submarine mud volcanos, which are important indicators for dynamic processes within gas bearing sedimentary units, are a common feature in marine environments and represent surface expressions of fluid flow and gas migration systems within the seafloor (Kopf 2002). Active mud volcanos show distinct geochemical signatures with changing salinity of pore fluids (Hensen *et al.* 2007). Also, large temperature gradients and occurrences of free gas (Feseker *et al.* 2009) can frequently be observed. Since the electrical resistivity of the seafloor is mainly determined by its porosity and the electrical resistivity of the pore fluid, the latter being weakly coupled to the temperature of the pore fluid (Fofonoff 1985), electromagnetic methods offer a promising approach to gain insight into a mud volcano's internal structure. Occurrences of fresh water, gas, gas hydrates or hydrocarbons decrease the saturation of the conductive pore fluid and, thus, lower the bulk resistivity. In addition the precipitation of authigenic carbonates to the seafloor at seep sites may appear as resistive anomaly, provided they form carbonate blocks or crusts which are sufficiently large with respect to the scale length of electromagnetic investigations. Consequently, a marine controlled source electromagnetic (mCSEM or CSEM from now on) experiment at 'North Alex', a mud volcano in the West Nile Delta, was scheduled to take place in November 2008.

The original plan for the CSEM experiment was to use the bottom towed system developed by the University of Toronto described in Schwalenberg *et al.* (2010) (Fig. 1, bottom panel). In preparation of the experiment it became clear that this system would not be suitable for investigations, since occurrences of carbonates, existing cable installations and various deployed scientific instruments would not have allowed for a safe operation.

For investigations at the North Alex we therefore had to implement a novel type of experiment, for which we used a remotely operated vehicle (ROV) to deploy the transmitter (Fig. 2). The experimental setup was inspired by the up to then unique CSEM experiment conducted at the TAG hydrothermal mound by Cairns *et al.* (1996). They had used the submersible *Alvin* to deploy a stationary, autonomous receiver onto the TAG hydrothermal mound.
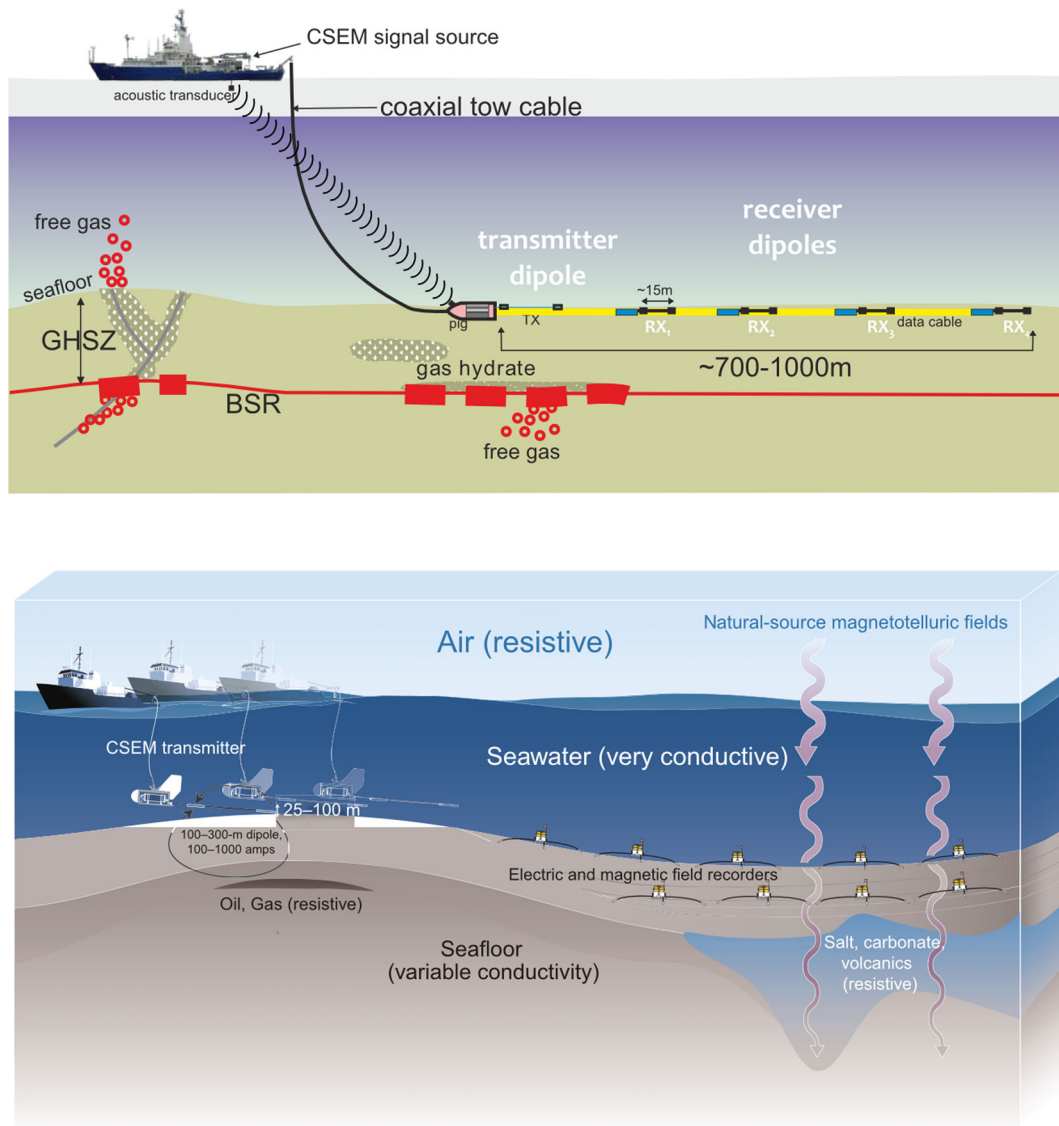
Figure 1. Conventional CSEM experiments with a cable-based system with fixed geometry (top panel, from Schwalenberg *et al.* 2010) or a 'flying' source and a stationary receiver array (bottom panel, from Constable 2010).
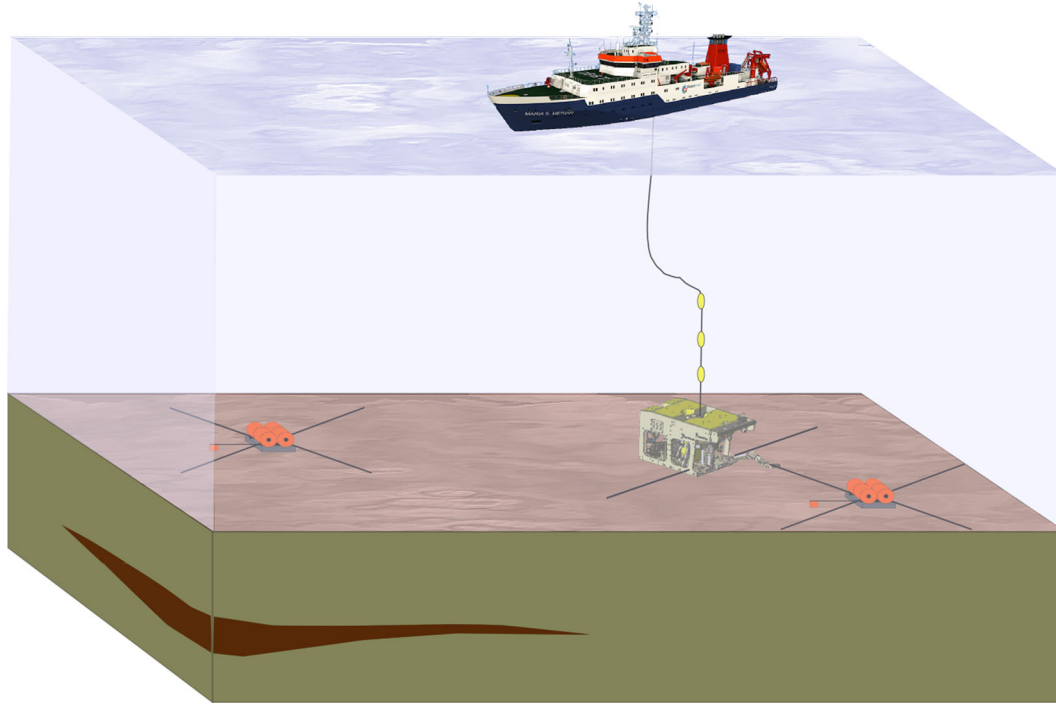
Figure 2. Schematic sketch of WND experiment with the ROV deployed transmitter and two nodal receivers (instruments are shown in Fig. 10). In the experiment transmitter and receivers are arbitrarily oriented. A sketch of the general geometry of the experiment is given in Fig. 3. Modified from Sommer *et al.* (2013).

Alvin was then used to move a transmitter around in the survey area. Their original plan to deploy both receiver and transmitter with two perpendicular antennas (3 m) each, had to be abandoned due to technical problems. Instead, the experiment was carried out with only one dipole on each, receiver and transmitter. The transmitter was operated with a single transmitter polarization at each site only (Cairns & Edwards, personal communication, 2014).

Apart from avoiding the hazards mentioned above, this style of experiment, where a submersible or ROV is used to move around the transmitter, offers the unique chance to excite several polarizations at every transmitter site. This is quite different to the bottom towed system (Fig. 1, top panel), which is only capable of exciting a single polarization at each transmitter site as well as for other common CSEM systems like the Scripps system described in Constable (2010) (Fig. 1, bottom panel), newer developments like the Vulcan System (Weitemeyer & Constable 2010) or the surface towed system described by Anderson & Mattson (2010). Generally speaking, the Scripps system could also be used in experiments, where two transmitter polarizations are collected. However, this is not standard which is due to the fact that this requires a different style of CSEM experiment, in which cross tows across the receivers are used to excite the second polarization, which is costly to implement (Constable 2010).

For these common systems, which excite a single transmitter polarization at each location a first pass interpretation of measured fields at receiver stations is usually carried out using the radial component of the electric field, whereas the azimuthal data is often not considered. However, recent publications recognize the fact that the collection of both polarizations would generally be advisable, for example in terms of resolving possible effects of 3-D anisotropic structures (Newman *et al.* 2010).

Measurements with two transmitter polarizations require different ways of processing and interpretation for a first-pass interpreta-tion. We are currently establishing a work-flow for such data, which relies on the concept of rotational invariants. The work-flow is as follows:

1. Construction of rotational invariants from marine CSEM data measured with non-parallel transmitter polarizations.
2. Derivation of apparent resistivities from the invariant data.
3. Interpretation of rotational invariants in terms of 1-D layered models of the seafloor.
4. Dimensionality analysis of rotational invariants.
5. Interpretation of rotational invariants in terms of 3-D modelling and inversions.

The calculation of apparent resistivities from one of the rotational invariants, which is useful for the fast imaging of data (step 2), is published in a companion paper (Swidinsky *et al.* 2015). The dimensionality analysis (step 4) and the 3-D interpretation (step 5) are both work in progress and will be included in future publications.

Within this paper steps 1 and 3 are covered in two main sections:

The first section deals with theoretical aspects of rotational invariants, first demonstrating how rotational invariants are constructed from measured data (step 1). After introducing the general concept, the sensitivity of rotational invariants is tested on a basic 1-D model, which resembles the measurement geometry of CSEM measurements at the mud volcano and the model resolution in the interpretation of rotational invariants is compares to the resolution, which can be achieved in the interpretation of a data set, which uses a single transmitter polarization only.

In the second section of this paper a proof of principle for the invariant approach is given by application to the CSEM data acquired during an experiment at the 'North Alex' mud volcano. The results of the CSEM data are tied into results from seismics and additional geoscientific data and finally interpreted in terms of gas saturation levels and structural features of the mud volcano.

ROTATIONAL INVARIANTS

Theory

Considering a CSEM experiment with two non-aligned transmitter (TX) dipoles with dipole moments $\mathbf{P_1}$ and $\mathbf{P_2}$ at a given TX location (Fig. 2, top panel), it is immediately clear that field components at a given receiver (RX) are usually not recorded as unique radial ($\mathbf{E_r}$) or azimuthal ($\mathbf{E_{az}}$) fields, but rather four trigonometric combinations of these fields (Constable & Cox 1996).

Of course it is possible to simply reconstruct the radial as well as the azimuthal component for each of the two transmitter polarizations. However, for a first-pass 1-D interpretation this poses two problems:

1. For a given transmitter location, the reconstructed radial and/or azimuthal components may not be unique and instead may differ substantially for the two polarizations $\mathbf{P_1}$ and $\mathbf{P_2}$. This can be due to the 3-D resistivity distribution of the subsurface, bathymetric effects or the change in source strength for a given direction (e.g. in the radial direction) for the two transmitter polarizations.

2. The flexible placement of the TX leads to a situation where polarization directions for adjacent TX locations may vary quite substantially (compare Fig. 8), that is when comparing a given polarization from one TX location to the next the measurement error of the reconstructed radial and/or azimuthal components may vary substantially because of the changing polarization direction.

Therefore, it is advantageous to find a representation of the measured field components, which is independent of the TX and RX orientations. This is possible by the use of rotational invariants, which were introduced for land-based dc measurements by Bibby (1977, 1986), applied by Risk *et al.* (1993) and further generalized to time-domain measurements by Caldwell & Bibby (1998). The aforementioned authors use an approach, in which the measured electric field components, which are excited by two (or more) non-aligned TX polarizations, are normalized by the dc current density. For land-based measurements over a half-space the dc current density is independent of the distribution of resistivities in the subsurface and the authors show that the determinant of the normalized E-fields can be interpreted in terms of apparent resistivities.

A direct adaption of this concept to the marine case fails—at least in terms of producing reasonable apparent resistivities—because in the marine case the dc current flow is not independent of the resistivity of the lower half-space. However, Li & Pedersen (1994) point out that the overall concept for rotational invariants, that is the independence on the choice of the reference frame, does not depend on the general distribution of resistivities. Thus, we argue that the general framework of rotational invariants, which was derived for land-based measurements, will also hold for the marine case. In this paper, we will show that rotational invariance can be established for the marine case, since it is only necessary to normalize the measured fields by a quantity, which reflects the source geometry. In the aforementioned companion paper we show how these invariants can be used to derive an apparent resistivity, which can be used for the quick imaging of CSEM data of experiments with two transmitter polarizations (Swidinsky *et al.* 2015).

Suppose we have an experiment, where a transmitter with two dipole polarizations and a receiver are placed horizontally onto the seafloor in an arbitrary geometry (Fig. 2, right-hand side). We assume the reference frame to be aligned with the x- and y-components of the RX. For two non-aligned TX measurements with time dependent (not denoted explicitly) dipole moments $\mathbf{P_1}$ and $\mathbf{P_2}$ and mea-

sured electric fields $\mathbf{E_1}$ and $\mathbf{E_2}$, the according xy-components in this reference frame are written in matrix notation to derive a source normalized E-field $\mathbf{E^n}$:

$$\mathbf{P} = [\mathbf{P_1}\mathbf{P_2}] = \begin{bmatrix} P_{x,1} & P_{x,2} \\ P_{y,1} & P_{y,2} \end{bmatrix}$$

$$\mathbf{E} = [\mathbf{E_1}\mathbf{E_2}] = \begin{bmatrix} E_{x,1} & E_{x,2} \\ E_{y,1} & E_{y,2} \end{bmatrix} \rightarrow \mathbf{E^n} \equiv \mathbf{E} \cdot \mathbf{P}^{-1}. \quad (1)$$

The calculation of $\mathbf{P^{-1}}$ is always possible, because the two polarizations are assumed to be non-aligned and, thus, $\mathbf{E^n}$ is well defined. Please note that in the following the superscript 'n' always denotes the source normalization and not a mathematical power. For matrix elements (E_{ij} and P_{ij}), the first index ($i = x, y$) identifies the horizontal component, the second index ($j = 1, 2$) identifies the used TX polarization.

We now consider a second coordinate system, which is rotated by an arbitrary angle with respect to the first coordinate system by using the corresponding rotation matrix. If the distance between TX and RX is larger than approximately $5\times$ the length of the TX bipole, they may be considered as dipoles. In this case—due to the principle of superposition—the components of both $\tilde{\mathbf{P}}$ and $\tilde{\mathbf{E}}$ in the rotated coordinate system are described by applying the 2-D rotation matrix $\tilde{\mathbf{R}}$:

$$\tilde{\mathbf{P}} = \tilde{\mathbf{R}}^{-1} \cdot \mathbf{P} \quad \tilde{\mathbf{E}} = \tilde{\mathbf{R}}^{-1} \cdot \mathbf{E}. \quad (2)$$

The source normalized E-field matrix in the rotated coordinate system can be written as:

$$\tilde{\mathbf{E}}^n = \tilde{\mathbf{E}} \cdot \tilde{\mathbf{P}}^{-1} = \tilde{\mathbf{R}}^{-1} \cdot \mathbf{E} \cdot \mathbf{P}^{-1} \cdot \tilde{\mathbf{R}} = \tilde{\mathbf{R}}^{-1} \cdot \mathbf{E^n} \cdot \tilde{\mathbf{R}}. \quad (3)$$

It is important to note that it is the normalization by the source polarizations, which ensures that $\mathbf{E^n}$ is a second-rank tensor, similar to the rationale used in the definition of the apparent resistivity tensor by Caldwell & Bibby (1998). Even though the elements of the source normalized E-field tensor depend on the orientation of the coordinate system, rotational invariants can be defined, which are indeed independent of the orientation of the coordinate system:

$$I_1 \equiv \det(\mathbf{E^n}) = \det(\tilde{\mathbf{E}}^n) = E_{x,1}^n \cdot E_{y,2}^n - E_{x,2}^n \cdot E_{y,1}^n$$

$$I_2 \equiv \text{trace}(\mathbf{E^n}) = \text{trace}(\tilde{\mathbf{E}}^n) = E_{x,1}^n + E_{y,2}^n \quad . \quad (4)$$

$$I_3 \equiv \text{skew}(\mathbf{E^n}) = \text{skew}(\tilde{\mathbf{E}}^n) = E_{x,2}^n - E_{y,1}^n$$

Additionally, we can use a combination of I_{1-3} to define I_4, which is also rotationally invariant:

$$I_4 \equiv I_2^2 + I_3^2 - 2I_1 = ||\mathbf{E^n}||^2 = \sum (E_{i,j}^n)^2. \quad (5)$$

This invariant is simply the sum of squares of the matrix elements as defined in eq. (1). It has the advantage that it has the same dimension as I_1 and we will later use it in the interpretation of data.

In order to calculate invariants for simple 1-D cases, we may assume a simple geometry as in Fig. 3, in which both TX and RX are aligned with the reference frame. The matrix of source normalized electric field components then simply contains the inline and broadside responses and rewriting eq. (4) yields:
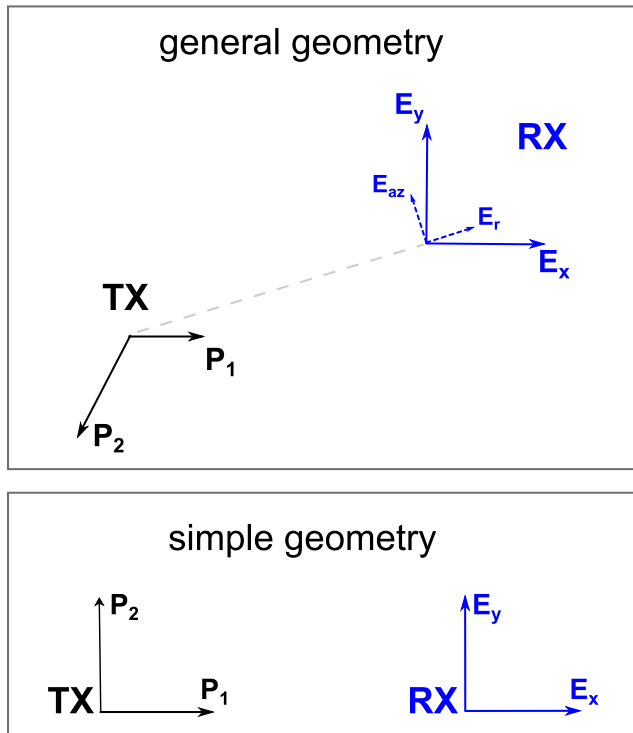
$$I_1 = E_{in}^n \cdot E_{br}^n$$

$$I_2 = E_{in}^n + E_{br}^n$$

$$I_3 = 0 \quad (6)$$

$$I_4 = (E_{in}^n)^2 + (E_{br}^n)^2,$$

Figure 3. Map view of the general geometry (top panel) of the experiment depicted in Fig. 2. Note that for the concept of rotational invariants, the two transmitter polarizations (P_1 and P_2) are only required to be non-parallel. Thus, the polarizations are depicted at a non-orthogonal angle and with different lengths for general considerations. However, in the CSEM experiment at the mud volcano the two polarizations were always nearly orthogonal and of equal dipole moment. For the calculation of rotational invariants for 1-D models we use a simple geometry (bottom panel), in which the transmitter and receiver are aligned with the reference frame. Here, polarization P_1 excites the pure inline response in receiver component E_x and polarization P_2 excites the pure broadside response in receiver component E_y.

where the superscript 'n' denotes the source normalization. For the 1-D case, the skew (I_3) is always zero. Since we will only interpret data in terms of 1-D layered earth models in the scope of this paper, the skew invariant will not be part of the interpretation presented here, but will be evaluated within a future 3-D interpretation of the data.

It is worthwhile to note that invariants I_1 and I_4 do not depend on the orientation of the receiver. For invariant I_1 this is easy to see, since applying a rotation matrix $\mathbf{R}$ to $\mathbf{E}^n$ and applying the definition of I_1 (4) yields:

$$\widetilde{I_1} = \det(\mathbf{R}\,\mathbf{E}^n) = \det(\mathbf{R}) \cdot \det(\mathbf{E}^n) = \det(\mathbf{E}^n) = I_1. \tag{7}$$

Thus, any error in the orientation of the system does not propagate into these invariants.

Model curves and sensitivity study

In the following we will use (6) for calculations of invariants, thus, all calculations presented hereafter are based on the assumption of a 1-D layered lower half-space representing the seafloor and a 1-D layered upper half-space, which represents the water column with the confining air layer above. For calculations we use a Fortran code originally developed at the University of Toronto, which implements the theory described in Edwards (1997) and Scholl & Edwards (2007). We have modified the code to allow for calcula-

tions with layered water columns and adapted the code to be directly accessible from within Matlab. For inversions, which we will show in a later section, we use the 1-D forward code in combination with the optimization method *lsqnonlin* from the Matlab Optimization Toolbox, which relies on a trust-region-reflective algorithm that is based on the interior-reflective Newton method described in Coleman & Li (1994, 1996).

To demonstrate how these invariants behave (Fig. 4), we will first consider a basic model, in which the resistivity of the lower half-space (representing the seafloor) is varied from 1 to 5 Ωm and the resistivity of the upper layer (representing the water column) is fixed at 0.3 Ωm (Fig. 5). The model resembles the most basic model, a double half-space, since the upper layer is thick compared to the RX–TX separation and, thus, the influence of the air-wave becomes negligible. Clearly, a sensitivity to the resistivity of the seafloor is given, which is not too surprising if one looks at the way the invariants may be calculated from the pure inline and broadside responses in eq. (6). To get further insight into how the interpretation of invariants compares to the standard interpretation of the radial (inline) and/or azimuthal (broadside) component(s), we will look at the sensitivity of transient responses to the parameters in terms of the *eigenparameter analysis* described in Edwards (1997). Additional application examples of the analysis can be found in Scholl & Edwards (2007) and Swidinsky *et al.* (2012). Contrary to the aforementioned authors we will not use the term eigenparameter (and derived terms) but rather singular value (SV) (and derived terms), because ultimately the analysis is based on the singular value decomposition (SVD) of a scaled Jacobian matrix, which is usually non-square. We will give a summary of the analysis described in Edwards (1997) and refer the reader to his article and the aforementioned references for further details and examples:

Suppose we have a measurement configuration and a given earth model—for example one similar to the one depicted in Fig. 5—with model parameters m_j ($j = 1, \ldots, N$), which represent layer thicknesses and resistivities, and a corresponding data vector $f_i(m)$ ($i = 1, \ldots, M$), which represents the measured transient response at one or more receivers. For such a configuration small variation dm_j in a model parameter m_j can be related to the changes df_i in the datum f_i by the first term of Taylor's series as

$$df_i = \sum_{j=1}^{N} J_{ij}\,dm_j \Leftrightarrow \delta\mathbf{f} = \mathbf{J}\,\delta\mathbf{m}. \tag{8}$$

Here, the coefficients J_{ij} are the partial derivatives $\partial f_i/\partial m_j$ in the Jacobian matrix $\mathbf{J}$. They connect the perturbation of the model-vector $\delta\mathbf{m}$ to the perturbation of the data vector $\delta\mathbf{f}$. Thus, they are a measure of the sensitivity of the data to the model parameters. Generally, this sensitivity in $\mathbf{J}$ can be analysed with the SVD:

$$\mathbf{J} = \mathbf{U}\mathbf{S}\mathbf{V}^{\mathbf{T}}. \tag{9}$$

In the *SVD* the $M{\times}N$ matrix $\mathbf{J}$ is decomposed into the unitary $M{\times}N$ data matrix $\mathbf{U}$, the diagonal $N{\times}N$ matrix $\mathbf{S}$, which contains the singular values (*SV*) along the diagonal S_{jj}, and the unitary $N{\times}N$ parameter matrix $\mathbf{V}^{\mathbf{T}}$. Note that since $\mathbf{U}$ and $\mathbf{V}$ are unitary, $\mathbf{U}^{\mathbf{T}} = \mathbf{U}^{-1}$ and $\mathbf{V}^{\mathbf{T}} = \mathbf{V}^{-1}$. The row vectors of $\mathbf{V}^{\mathbf{T}}$ are called SV-parameters, (SV_{par}) which contain the information on how specific combinations of model parameters are mapped from the model space into the data space in terms of the SVD analysis. The importance of each SV-parameter is determined by the corresponding singular value on the diagonal of $\mathbf{S}$. This can be seen by rewriting and rearranging (8) using (9):

$$\mathbf{U}^{\mathbf{T}}\delta\mathbf{f} = \mathbf{S}\mathbf{V}^{\mathbf{T}}\delta\mathbf{m}. \tag{10}$$
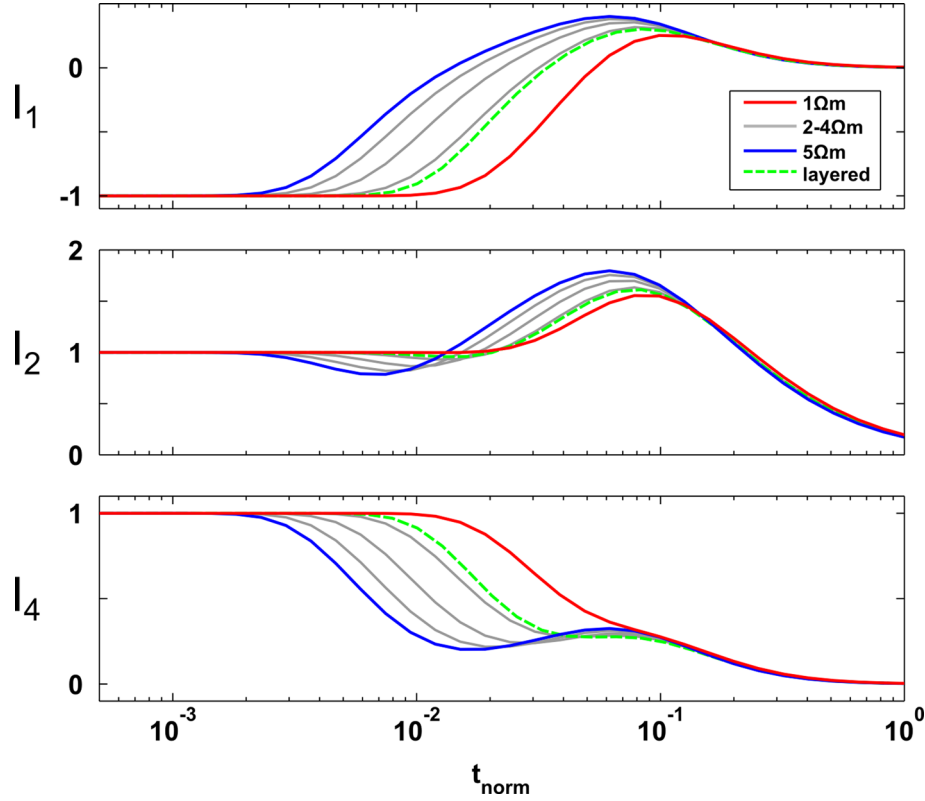
Figure 4. Invariants for homogeneous lower half-spaces with a thick upper water layer, which essentially resemble double half-spaces. Lower half-space resistivities, which represent the seafloor, range linearly from 1 Ωm (red) to 5 Ωm (blue), intermediate values are depicted by grey lines. The resistivity of the upper halfspace, which represents the water column, is fixed at 0.3 Ωm. For ease of comparison, amplitudes of invariants are normalized to the absolute value of their dc offsets. Similar to Edwards & Chave (1986) we display time as dimensionless normalized time ($t_{norm} = t / \tau$), where normalization is performed with respect to the characteristic time of seawater $\tau = \mu_0 \, \sigma_0 \, r^2$ ($r \rightarrow$ TX–RX offset; $\sigma_0 \rightarrow$ conductivity of the water column). Green lines show invariants of the layered model depicted in Fig. 5. Due to the normalization they look similar to the invariants of a homogeneous 2 Ωm lower half-space, but indeed have different amplitudes.

Edwards (1997) shows how the error in each SV-parameter can be expressed in terms of the above analysis: if each datum f_i of the data set has an independent standard error estimate e_i of unity, the standard error $\Delta(SV_{par})$ of a SV-parameter in terms of the model variation is just the reciprocal of the corresponding singular value:

$$\Delta \left(SV_{par} \right) = \mathbf{V^T} \delta \mathbf{m} = \mathbf{S}^{-1}. \tag{11}$$

A coarse upper bound on the standard error Δ_{max} of the original model parameter m_j can also be given in terms of the entries of the V-matrix and the singular values:

$$\Delta_{max} \left(m_j \right) = \sum_{j=1}^{N} \left| \frac{V_{ij}}{S_{jj}} \right|. \tag{12}$$

However, an error in a model parameter may only be computed in this manner if it is small compared with unity because the theory described is only valid for linear changes.

Edwards (1997) points out that it is useful to scale the Jacobian **J** for a given earth model and measurement geometry in two ways before performing the analysis. First, each coefficient J_{ij} is scaled by the corresponding standard errors e_i. This has the effect of rescaling the units in which datum f_i is measured such that its standard error is unity, which is required in the derivation of (11). Secondly, each coefficient J_{ij} is multiplied by the corresponding model parameters m_j,

thus, redefining the parameter m_j as log(m_j) ($\rightarrow$ natural logarithm), because

$$m_j \frac{\partial f_i}{\partial m_j} = \frac{\partial f_i}{\partial \log \left(m_j \right)}. \tag{13}$$

With this scaling the estimates on the upper bounds of the standard errors (12) become estimates on the fractional standard errors in the model parameters, which we will denote as δ_{max}. The same applies to the standard errors of the SV-parameters, which we will denote as δSVpar.

We apply the sensitivity analysis to model responses of the 1-D model depicted in Fig. 5, which resembles a measurement geometry and plausible underground model for the CSEM measurements at the North Alex. This model has four model parameters, namely the background resistivity of the seafloor ρ_1, the resistivity and thickness of an embedded resistive layer (ρ_2 and d_2, respectively) and the thickness of the seafloor above this embedded layer (d_1). For this model, transient step-off responses for the inline and broadside configuration (E_{in} and E_{br}, respectively) and the corresponding Jacobians ($\mathbf{J_{in}}$ and $\mathbf{J_{br}}$, respectively) are calculated numerically for two receivers on the seafloor, which are located at distances of 150 and 300 m from the transmitter. The Jacobians of the rotational
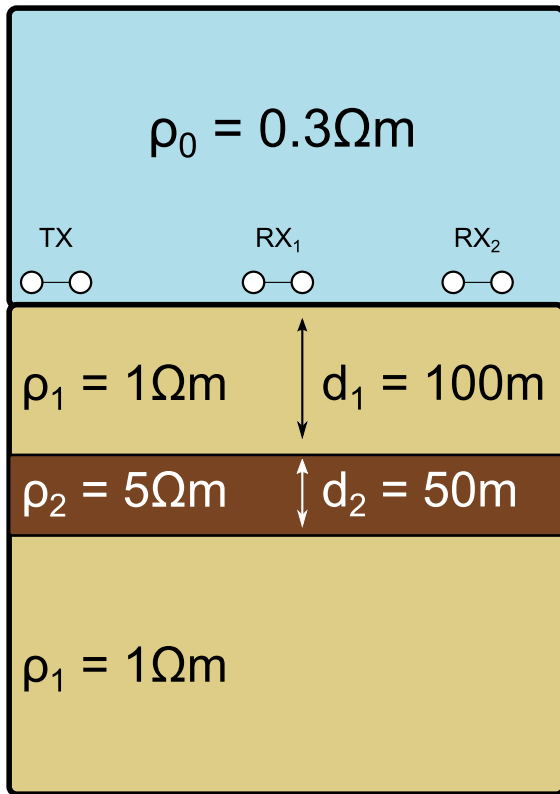
Figure 5. Basic 1-D model used for the SVD analysis in Fig. 6. It consists of a 50-m-thick resistive layer (5 Ωm), which is embedded into a regular seafloor (1 Ωm). The water layer is chosen to be very thick with respect to the TX–RX offsets and, thus, the air layer is not depicted. Two receivers are located at distances of 150 and 300 m from the transmitter. Responses from both receivers are used in the SVD analyses. For the analyses displayed in Fig. 7 the thickness of the first layer (d_1) is varied between 50 and 200 m.

invariants can easily be derived from (6) by applying the partial derivatives with respect to the model parameters:

$$
\begin{aligned}
\mathbf{J}\left(\mathbf{I}_1\right) &= \operatorname{diag}\left(E_{in}\right) \cdot \mathbf{J}_{\mathbf{br}} + \operatorname{diag}\left(E_{\mathrm{br}}\right) \cdot \mathbf{J}_{\mathbf{in}} \\
\mathbf{J}\left(\mathbf{I}_2\right) &= \mathbf{J}_{\mathbf{in}} + \mathbf{J}_{\mathbf{br}} \\
\mathbf{J}\left(\mathbf{I}_4\right) &= 2 \cdot \left[\operatorname{diag}\left(E_{\mathrm{in}}\right) \cdot \mathbf{J}_{\mathbf{in}} + \operatorname{diag}\left(E_{\mathrm{br}}\right) \cdot \mathbf{J}_{\mathbf{br}}\right]
\end{aligned}
\tag{14}
$$

To perform the analysis, we assume the standard error e for each measurement and channel to be uncorrelated and distributed normal at each time step t_i:

$$
e\left(t_i\right) = 0.01 \cdot E_i + 10^{-11} \cdot t_i^{-1/2}\left(\frac{\mathrm{V}}{\mathrm{Am}^2}\right).
\tag{15}
$$

Here, E_i is the measured source normalized electric field at each time step t_i. This error has two contributions. The first contribution is a relative error expressed as a percentage of the amplitude, which could account for uncertainties in the measurement geometry or instrumental errors and is assigned to be 1 per cent for this sensitivity study (similar in Brown *et al.* 2012 or Edwards 1997). The second contribution, is inversely proportional to the square root of time. This form of noise dependence is common for transient electromagnetic data which is processed by 'log-gating' and 'gate stacking'. Here, 'log-gating' refers to an integration of transients over time gates with equal length on a logarithmic timescale and 'gate stacking' refers to the subsequent stacking of all gates with the same time delay (Munkholm & Auken 1996). For the transient step-off responses considered here, this contribution is negligible

at early times, but becomes significant at late times. It prevents an unrealistic dominant effect of small voltages at late times of the transient. According to the measured noise floors during the experiment, we assume that this time dependent contribution reaches a source normalized level of 10^{-11} V/Am^2 at 1 s.

Prior to the SVD-analysis, the Jacobians are scaled to the model parameters (d_1, d_2, ρ_1, ρ_2) and to the standard errors as in the derivation by Edwards (1997). For the inline and broadside fields we use standard errors (e_{in} and e_{br}, respectively) as defined in (15). We assume these standard errors to be uncorrelated and derive the according standard errors of the invariants from eq. (6) via error propagation:

$$
\begin{aligned}
e_{\mathrm{I}_1} &= \left(\left(E_{\mathrm{br}} \cdot e_{\mathrm{in}}\right)^2 + \left(E_{\mathrm{in}} \cdot e_{\mathrm{br}}\right)^2\right)^{1/2} \\
e_{\mathrm{I}_2} &= \left(e_{\mathrm{in}}^2 + e_{\mathrm{br}}^2\right)^{1/2} \\
e_{\mathrm{I}_4} &= 2 \cdot \left(\left(E_{\mathrm{in}} \cdot e_{\mathrm{in}}\right)^2 + \left(E_{\mathrm{br}} \cdot e_{\mathrm{br}}\right)^2\right)^{1/2}
\end{aligned}
\tag{16}
$$

In a similar manner, errors from real measurements with arbitrarily oriented transmitter and receiver can be derived from eqs (4) and (5), again under the assumption that errors for the four measured signals are uncorrelated.

In Fig. 6 SVD-analyses are displayed for the scaled Jacobians of the pure inline and pure broadside responses (top row) and for scaled Jacobians of combinations of rotational invariants I_1, I_2 and I_4 (bottom row). We will explain the result and display of the analysis in detail for the inline response (top left-hand side):

The main axis displays the coefficients of the parameter matrix $\mathbf{V}^{\mathrm{T}}$ with circles of radii, which are proportional to the coefficients. Positive and negative coefficients are shown as red and blue circles, respectively. Each row contains one SV-parameter and the displayed coefficients are the weights of the original model parameters within the according SV-parameter. The original model parameters are noted above the top axis. Within $\mathbf{V}^{\mathrm{T}}$ the SV-parameters are sorted with the most important, that is the one with the largest SV, located in the top row and least significant, that is the one with the smallest SV, being located in the bottom row. SV are normalized with respect to the largest SV and we use opacity along rows to show the importance of each SV-parameter: the top row with a normed SV of unity is completely opaque and rows 2–4 with SVs < 1 become increasingly transparent. Please note that the SV is not explicitly noted in the plots. Instead we display the fractional standard error of each SV-parameter ($\delta \mathrm{SV}_{\mathrm{par}}$) along the y-axis, which is simply the reciprocal of the SV. Estimates on the upper bound of the fractional errors of logarithmic model parameters ($\delta_{\max}$) are given along the lower axis of the plot.

The first and second SV-parameters in the top two rows (Fig. 6, 'inline') each have one dominant entry, which are associated with the model parameters ρ_1 and d_1. The fractional errors on the according model parameter are $\delta_{\max}(\rho_1) = 0.10$ and $\delta_{\max}(d_1) = 0.22$. Thus, the original model parameters ρ_1 and d_1 should be resolved better than ± 0.1 Ωm ($= 1$ Ωm $\times 0.10$) and ± 22 m ($= 100$ m $\times 0.22$). The third and fourth SV-parameter are no longer associated with a single model parameter, but rather combinations of model parameters ρ_2 and d_2. Remembering that we have used log-scaling on the model parameters, we can use (11) for the 3rd SV-parameter:

$$
\Delta(\mathrm{SV}_{\mathrm{par}}) \approx V_{23} \cdot d \log\left(\rho_2\right) + V_{43} \cdot d \log\left(d_2\right).
\tag{17}
$$

Thus, the physical interpretation of this eigenparameter may be deduced as

$$
\rho_2^{V_{23}} \cdot d_2^{V_{43}}.
\tag{18}
$$
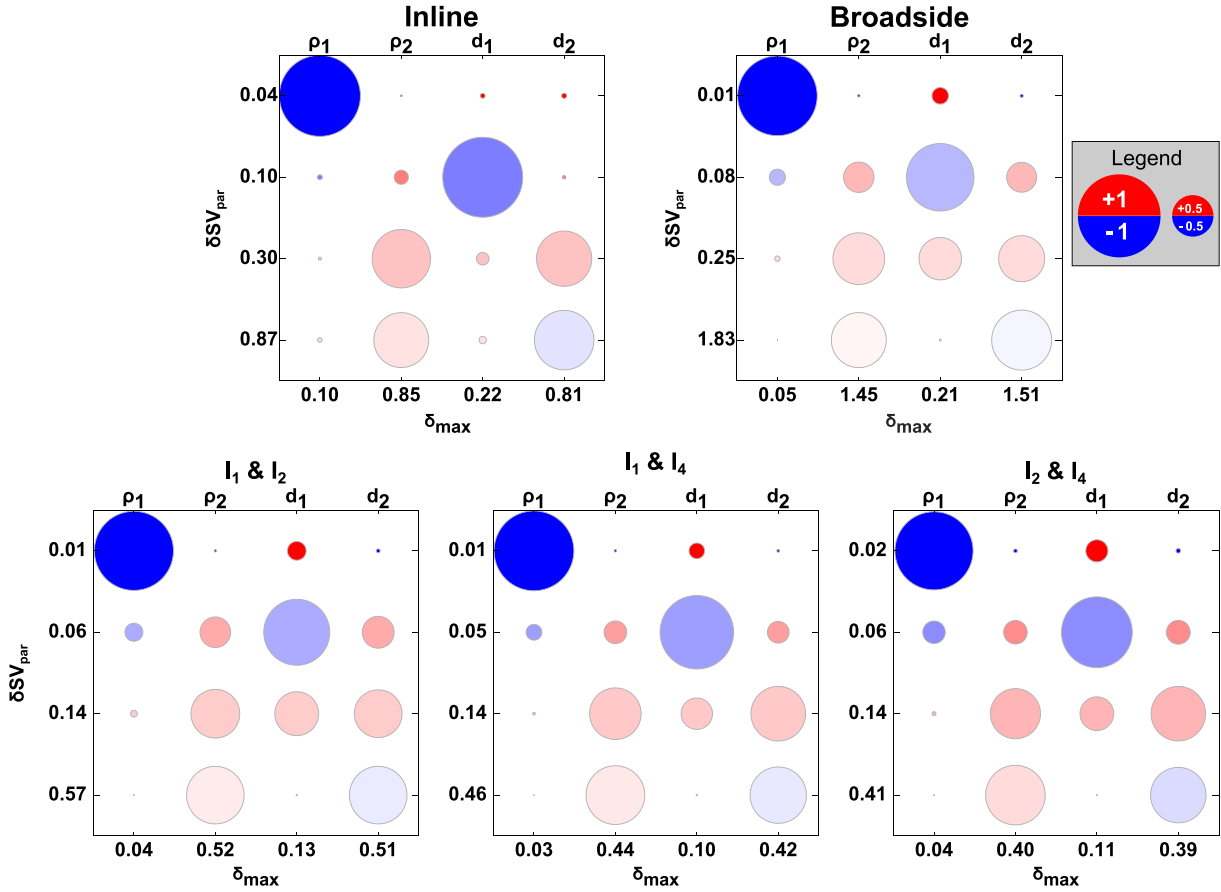
Figure 6. Graphical display of SVD-analyses performed on scaled Jacobians, which contain the sensitivity for the CSEM configuration and 1-D model depicted in Fig. 5 (top panel: pure inline and pure broadside; bottom panel: combinations of rotational invariants I_1, I_2, I_4). In each subplot, the radius of circles is proportional to the coefficients of matrix $\mathbf{V}^{\mathrm{T}}$ and positive and negative values are assigned the colours red and blue, respectively. Along each row the opacity of circles is scaled proportional to the corresponding singular value (SV). Because SVs are sorted and normed to the largest SV, the top row is completely opaque and transparency increases towards the bottom row. Along the y-axes we show the standard errors of the SV-parameters (ΔSV_{par}), which is the reciprocal of the corresponding SV (Edwards 1997). Along each bottom *x*-axis the estimates of the upper error bounds (δ_{max}) on the original parameters as calculated by eq. (12) are shown. The corresponding original model parameters are denoted along the top *x*-axis. Note that analyses are performed on log model-parameters as explained in the text.

Since both coefficients V_{23} and V_{43} have the same sign, this is the resistivity-thickness product of the embedded resistive layer. In a similar manner, the 4th SV-parameter contains the quotient of these model parameters, since V_{24} and V_{44} have opposite signs. Generally speaking, the two model parameters could be resolved independently with the 3rd and 4th SV-parameter, provided the corresponding errors are small enough. However, for the inline response the according error estimates are close to unity [$\delta_{max}(\rho_2) = 0.85$; $\delta_{max}(d_2) = 0.81$]. Thus, the assumptions made in the derivation by Edwards (1997) do not hold and the parameters cannot be considered to be resolved within the scope of the analysis performed here.

When comparing the inline response to the broadside response (Fig. 6, top right-hand side) it becomes clear that the broadside response is less suitable to determine the model parameters. According to the first SV-parameter, ρ_1 is resolved well (± 0.05 Ωm), but the interdependence/mixing within the other SV-parameters is significant and the estimated upper error bounds on the parameters of the embedded layer are significantly higher. This is the reason why the radial/inline configuration is generally the preferred choice in detecting resistive structures (Constable 2010).

Generally, for an experiment with two TX polarizations (Fig. 2) all invariants can be calculated and may thus be jointly interpreted.

Therefore, we will compare the pure inline and broadside (Fig. 6, top row) to combinations of two invariants (Fig. 6, bottom row). Again, all analyses were based on the same basic 1-D model and geometry as depicted in Fig. 5 and measurement errors from the inline and broadside were propagated to the invariants via eq. (16). It is evident that the analyses of combinations of invariants significantly reduce the errors of the SV-parameters (δSV_{par}) and the upper error bounds of model parameters (δ_{max}) as compared to the pure inline or pure broadside alone. The best resolution is given by combinations of invariants I_1 and I_4 (bottom middle) and invariants I_2 and I_4 (bottom right-hand side). For these invariants the upper error bounds of model parameters (δ_{max}) are almost identical and absolute upper error bounds on the parameters are:

I_1 and I_4 : $\Delta\rho_1 = \pm 0.03\,\Omega\mathrm{m}$, $\Delta\rho_2 = \pm 2.22\,\Omega\mathrm{m}$,
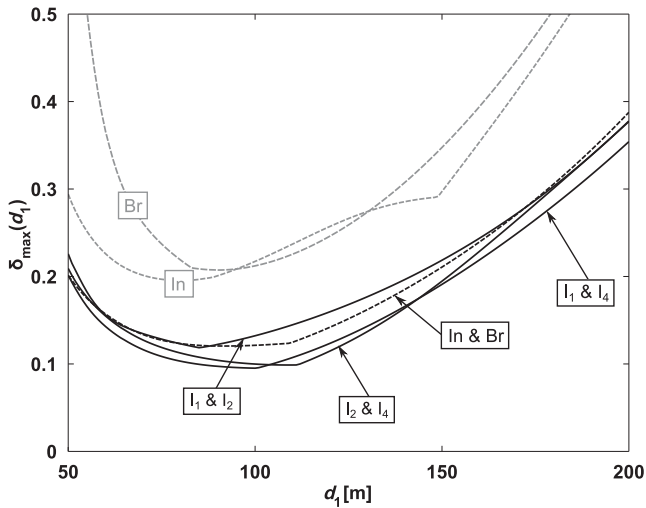
$$\Delta d_1 = \pm 5\,\mathrm{m}, \ \text{and}\ \Delta d_2 = \pm 21\,\mathrm{m},$$

I_2 and I_4 : $\Delta\rho_1 = \pm 0.04\,\Omega\mathrm{m}$, $\Delta\rho_2 = \pm 2.00\,\Omega\mathrm{m}$,

$$\Delta d_1 = \pm 11\,\mathrm{m}, \ \text{and}\ \Delta d_2 = \pm 19.5\,\mathrm{m}.$$

As mentioned before, the results presented so far apply to the 1-D model and measurement geometry depicted in Fig. 5 as well

Figure 7. Fractional error $\delta_{max}(d_1)$ for a varying thickness d_1 of the model depicted in Fig. 5. Errors derived from analyses of the inline (In) and the broadside (Br) responses and combined responses of invariants (I_1, I_2, I_4), are depicted in grey and black, respectively. Also shown are the errors for the combined inline and broadside response (In and Br), which are similar to those of the combined invariants.

as the assumed standard error of measurements in eq. (15). To show that these results also apply in a broader sense, we have repeated the analysis above for a whole set of models which are similar to the one depicted in Fig. 5. The only parameter that is changed is d_1, which we vary between 50 and 200 m, which practically means that we shift the depth of the embedded resistive layer. The essence of this model study is contained in Fig. 7, which shows the dependence of the fractional standard error for the model parameter d_1 for the given model set. Dashed grey lines show the standard errors, which relate to analyses of the pure inline and the pure broadside (In and Br in Fig. 7) and black solid lines the standard errors, which relate to analyses of combined rotational invariants (I_1 and I_2, I_1 and I_4, I_2 and I_4 in Fig. 7). It is immediately evident, that combinations of invariants always yield a better parameter resolution as compared to the pure inline or broadside. Looking at the combined invariants in detail, we see that combinations of invariants I_1 and I_4 and I_2 and I_4 yield similar error estimates over a wide range of models and usually perform better when compared to a combination of invariants I_1 and I_2.

We have also included the results for the simultaneous analysis of inline and broadside responses (In and Br in Fig. 7), for which the upper error bound is similar when compared to the combinations of two rotational invariants. This is to be expected, because for this study of sensitivities the rotational invariants are calculated from the inline and broadside responses using eq. (6). However, for a real measurement the rotational invariants offer the advantage to be determinable uniquely from any two, non-aligned transmitter polarizations, whereas the determination of radial and/or azimuthal components from two transmitter polarizations may not be unique, which poses a problem for the interpretation of data in terms of 1-D models.

Generally, the simultaneous interpretation of all three invariants is advisable for a real data set, but does not make sense in terms of the 1-D model studied here: for the 1-D case invariant I_4 depends solely on invariants I_1 and I_2 and is no longer independent, which can be seen by setting $I_3 = 0$ in eq. (5).

In summary, the analyses of sensitivities demonstrate that measurements with two TX polarizations lead to significant improve-

ments in the resolution of 1-D layered structures. It seems evident that the use of more than one transmitter polarization will also help to improve the model resolution for 2-D or 3-D resistivity structures (see for example Newman *et al.* 2010) and the concept of rotational invariants offers a convenient way to handle such data sets accordingly.

CASE HISTORY

### Geological setting of the North Alex Mud volcano

The 'North Alex' mud volcano is located about 50 km to the North of Alexandria (Egypt) in the West Nile Delta (WND). The bathymetry of the central crest with a diameter of ~1 km is rather flat topped with water depths ranging between 500 and 515 m over the main crest (Fig. 8). From previous remotely operated vehicle (ROV) dives it was known that ridges and troughs with a considerable relief of about 3 m exist at small scales (Dupre *et al.* 2007). They are visible as small scale, concentric undulations around the centre of the mud volcano in the bathymetric map. While the mud volcano was found in a relatively dormant stage with little activity during two research cruises in 2003 and 2004, active degassing and very high temperatures of almost 70 °C at shallow depth of about 6 m were observed in 2008 (Feseker *et al.* 2010) during research cruise 64PE298 (R/V PELAGIA). During this research cruise, geophysical investigations (seismics and CSEM) were carried out to further investigate the internal structure of the mud volcano.

For the seismic experiment the source (105 in^3 GI gun) was towed 18 m behind the ship and operated with a shot interval of 7 s at a ship speed of three knots. Shots were recorded with a 100-m-long streamer with 32 channels. As an example, Fig. 9 shows an fk-migrated ($v_p = 1500$ m s^{-1}) CMP section, which was measured along a WSW–ENE striking profile across the centre of the mud volcano (Fig. 8).

The seismic section in Fig. 9 shows a pull down of the main seismic reflectors to either side of the mud volcano (CMP 700–900 and 1500–1600). The fact that not all refflectors are dipping to the same extent is not consistent with a pure velocity pull down effect, which should be similar for all refflectors or increasing with depth. Therefore, the pull down reflects, at least to some degree, a structural deformation. The interior of the mud volcano is mainly characterized by blanking in the central part of the mud volcano (CMP 1100–1200 in Fig. 9) and by incoherent scattering towards either side of this central part. Apart from the blanking and scattering, two prominent structural features are visible within the mud volcano:

The first marked feature in the seismic section (Fig. 9) is a reflector directly beneath the seafloor. The reverse polarity of this reflector implies a negative impedance contrast and is interpreted to represent the top level of gas saturation within the mud volcano, since considerable degassing was observed around the centre of the mud volcano. Since the *P*-wave velocity decreases for gas saturations between 0 and 10 per cent and then remains consistently low for concentrations above this level (Minshull *et al.* 2012), the reflector is indicative for the existence of gas but cannot yield quantitative estimates on saturation levels above 10 per cent.

The second feature, which is visible within the region of mostly incoherent scattering, is a reflector with normal polarity, which indicates an internal layer that can be interpolated to connect across the blanking zone to form a lens-shaped interface. According to the seismic section, this lens-shaped structure is approximately 1700 m
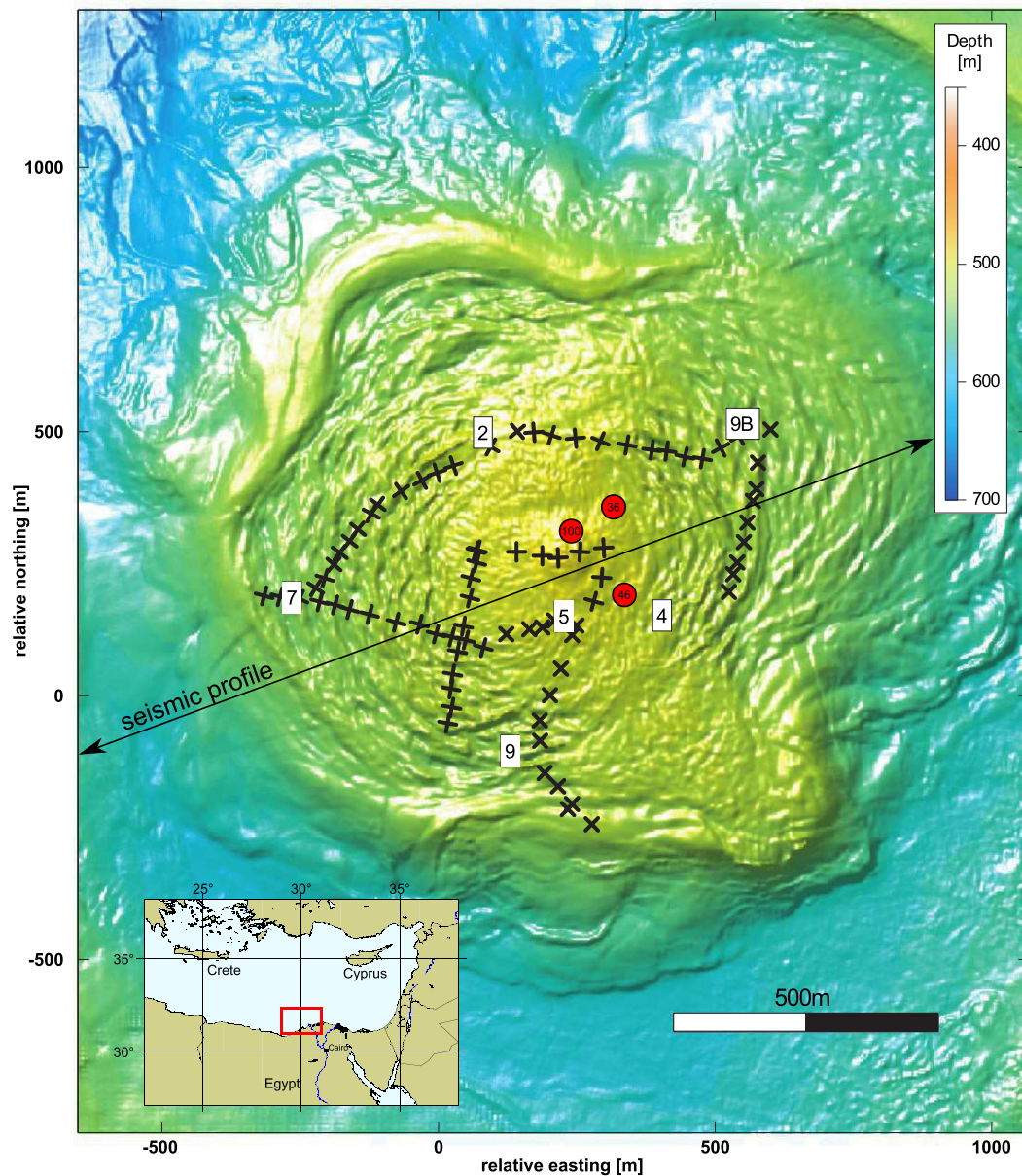
Figure 8. Bathymetic map of the North Alex mud volcano with locations of geoscientific investigations. The seismic section along the indicated profile is shown in Fig. 9. White boxes and crosses show the locations of the CSEM receiver and transmitter stations, respectively. The actual systems are shown in Fig. 10. Data samples from receiver 7 are shown in Fig. 11. Red circles mark the locations of three gravity cores, for which porosities and resistivity logs were taken in laboratory measurements (Fig. 17). Map after Feseker *et al.* (2010), changed. Bathymetric data was provided courtesy of BP.

wide and has a vertical extent of ∼0.18–0.2 s TWT with the base approximately between seismic CMP points 1125 and 1175 (Fig. 9). A remarkably similar section is described by Perez-Garcia *et al.* (2009) for the Håkan Mosby mud volcano (HMMV, see inlay in Fig. 9), which also show a pull down of reflectors towards the mud volcano, seismic blanking at and around the central conduit of the mud volcano and a lens-shaped feature centred beneath the mud volcano. At the HMMV the lens-shaped structure is slightly smaller with a lateral and vertical extent of ∼1400 m and ∼0.15–0.16 s TWT, respectively, but the overall geometry is strikingly similar. Perez-Garcia *et al.* (2009) interpret the lens-shaped structure as collapse structure, which formed after the initial 'birth' phase of rapid mud volcanism. After a phase of inactivity the collapse structure was refilled in subsequent phases of mud volcanism. Thus, the reflector would represent an older, potentially more compacted

and cemented surface of the mud volcano from an earlier phase of active mud volcanism.
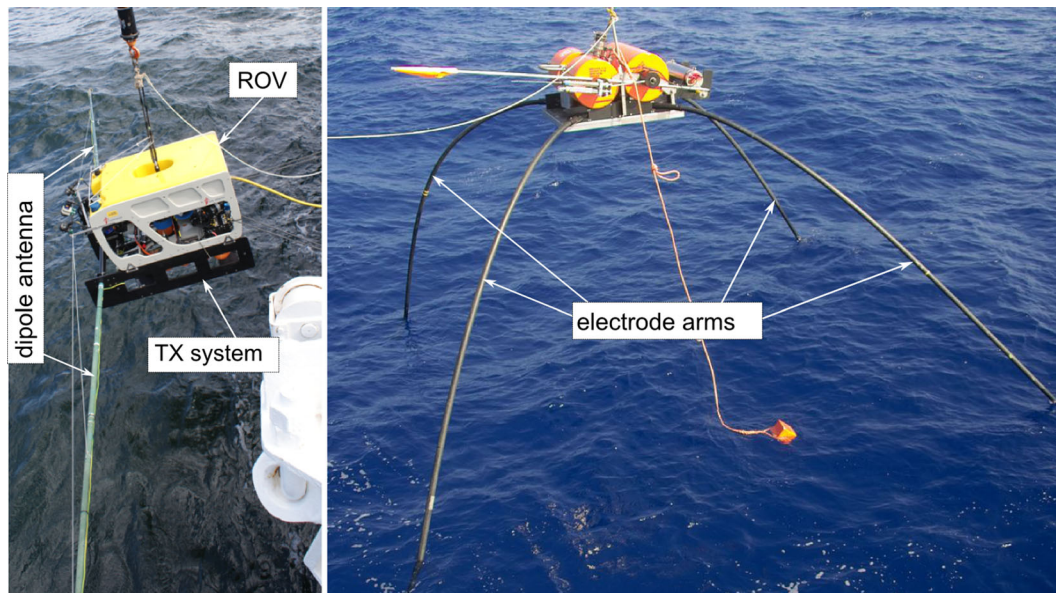
CSEM experiment

During the research cruise 64PE298 (R/V PELAGIA, 2008 November) we had the possibility to use a *Cherokee* remotely operated vehicle (ROV) operated by the Ghent University (Belgium) for scientific experiments. The basic idea was to perform an experiment similar to the one described by Cairns *et al.* (1996) to investigate the resistivity structure of North Alex.

The main challenge for the successful implementation of a CSEM experiment similar to the one originally tried by Cairns *et al.* (1996) was to build a transmitter system with a sufficiently large dipole
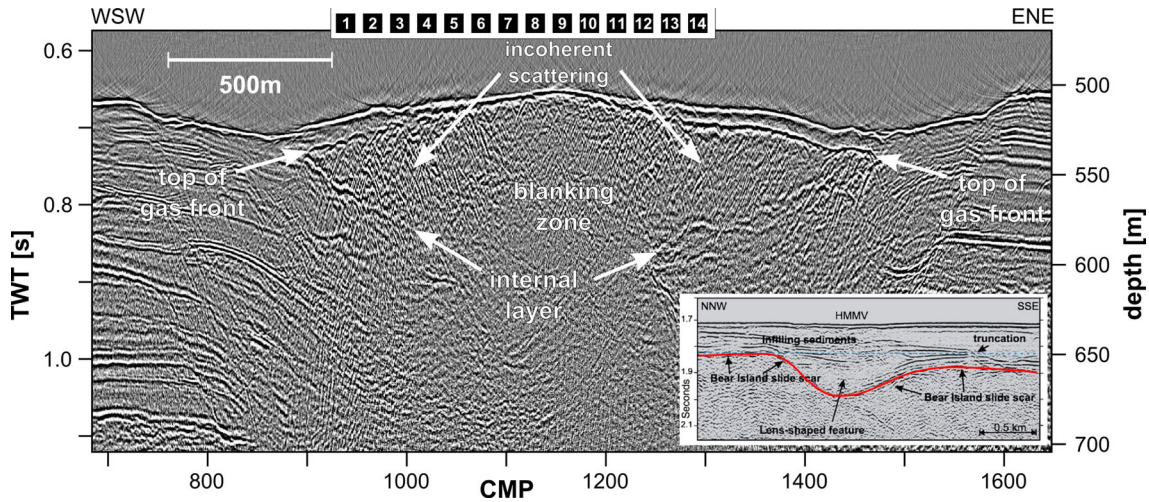
Figure 9. CMP stacked and fk-migrated (Stolt 1978) seismic section ($v = 1500$ m s^{-1}) along the profile line indicated in Fig. 8. For reference purposes, the numbering used for the CMP grid of the CSEM interpretation (compare Fig. 12 and Fig. 14) is indicated above the section. The inlay on the lower right-hand side shows a seismic section from the Håkan Mosby mud volcano (Fig. 2a from Perez-Garcia *et al.* 2009, changed) with a lens-shaped interface (red line), which is similar to the internal layer in the section from the North Alex mud volcano.

Figure 10. GEOMAR CSEM transmitter system and dipole antenna mounted to a Cherokee ROV (left-hand side). Nodal receivers (right-hand side) are deployed onto the seafloor to record the transmitted signals. The principal style of experiment is depicted in Fig. 2, a station map of the CSEM experiment in the WND and data samples can be found in Figs 8 and 11, respectively.

moment for the CSEM investigations at the mud volcano, which could still be handled by the small *Cherokee* ROV (size: 1.4 m × 0.9 m × 1.2 m, weight: 450 kg, payload: <10 kg) which is very small compared to Alvin (size: 7.1 m × 2.6 m × 3.7 m, weight: 7 t, payload: 680 kg), which was used during the experiment by Cairns *et al.* (1996). The limited payload posed a first important constraint for the development of a TX system. As an additional restriction the available power supply from the ROV was limited to about 150 W. According to these limitations the transmitter was designed to be powered from a battery pack. With a capacity of 5 Ah (@42 V) the battery pack had enough power to transmit a signal of about 23.6 A into an electric dipole antenna for several minutes. Since batteries were operated in a fast charging buffer mode, that is they were constantly recharged at an overvoltage of 52.5 V, they only needed about 1–2 min to recharge to full capacity after a

transmission cycles of up to 5 min. This was an acceptable compromise, since it was planned to only activate the transmitter with the ROV placed stationary onto the seafloor which left enough time for recharging while the ROV was to be moved from one station to the next. The transmitter (including the battery pack, dc–dc converters, H-bridge, electronics and a microcontroller unit, which allowed live control of the system using a RS232 serial interface) fit into a compact titanium pressure tube (Ø 160 mm, length 900 mm) with a negative buoyancy of about 10 kg in water. The pressure tube and floats, which compensated the weight of the pressure tube in water, were assembled in a small skid, which was mounted beneath the ROV (Fig. 10, right-hand side). Furthermore, two sailing masts with stainless steel electrodes at their ends were mounted to the skid as dipole antenna with a total length of 9.1 m. The assembled system is shown in Fig. 10 (left-hand side). The ROV also carried

a CTD probe, which constantly measured the conductivity of the water column. The data acquired by this CTD probe compared well with conductivity data from two CTD casts, which were performed at the centre and at the edge of the mud volcano prior to the CSEM experiment. The CTD data showed no significant lateral or temporal variations and we have used this data to derive a layered conductivity model of the water column, which was used for the subsequent interpretation of CSEM data.

For the CSEM experiment we used five receivers (Fig. 10, right-hand side), which were synchronized to GPS time prior and after the experiment. Each receiver is equipped with a three component fluxgate magnetometer, and can measure two components of the horizontal electric field. The components of the electric field are measured using Ag/AgCl-electrodes, which were attached at the end of four flexible arms. The total length of each receiver dipole is 10 m. Additional sensors allow measurements of the attitude (pitch, roll) and the temperature. The receivers can either be used in an MT-mode, in which all sensors are logged at sampling rates of up to 10 Hz, or switched into a CSEM-mode, in which only two components of the E-field are recorded at a high sampling rate of 10 kHz. This high frequency is necessary to acquire transient data at short offsets on the order of 100 m (compare Cairns *et al.* 1996). The switch from one mode to the other can be performed by using a pre-set timetable or alternatively by an external acoustic signal. The receivers were deployed by free fall in an array onto the main crest of *North Alex* (see Fig. 8). One of the receivers (RX9) was recovered after the first ROV dive in the southeastern and central part of the mud volcano to check that the system was working correctly. After verification, it was redeployed to a new location (RX9B) northwest of the centre, where later measurements were scheduled. Before and after the CSEM experiment the receivers were operated in MT-mode. A comparison of the average total magnetic field values measured at receiver sites to the reference earth magnetic field of about 43 600 nT shows deviation of up to 1000 nT. Recent tests have shown that these deviations are mainly due to steady magnetic fields of releases (batteries, motor) and the influence of the steel anchor bars, which were used to connect the anchor weight to the release. Therefore, we have used the acquired magnetometer data to determine the heading of stations, but it is evident that these headings are biased to some degree. This bias could be mitigated by deriving a heading through coherency analysis of magnetic field variations at different rotation angles between stations and land observatory data. However, in the context of this paper, where we rely on the analysis of rotational invariants, it is not relevant to pursue this issue further. According to the receivers' internal attitude sensors, the frames of all receiver stations came to rest in a stable position. For each receiver station, the final pitch and roll were below 8° with respect to the horizontal. The available video footage from the ROV also suggests that electrode arms were spread out straight onto the seafloor. Measurements of the ambient noise floor yielded typical values of about 2×10^{-8} V/$\sqrt{Hz}$. With the given transmitter dipole moment of ∼215 Am and the receiver dipole length of 10 m this yields a noise floor of 10^{-11} V/(Am$^2\sqrt{Hz}$) for the source normalized E-field components.

The actual CSEM experiment was carried out during three ROV dives, which took place 4, 6 and 8 d after the deployment of receivers. With the maneuverability of the ROV it was possible to operate the transmitter at a total of 80 locations (see Fig. 8). At each location the transmitter was activated twice for 1 min with a bipolar, rectangular waveform (± 23.4 A, 50 per cent duty-cycle, 0.25 Hz, ramp time <0.1 ms), once aligned and once perpendicular to the current profile direction. Thus, the measurement cycle for each transmit-

ter polarization contained 15 full switching cycles. The transmitter was placed at locations with a spacing of about 40 m on profile lines connecting the receiver locations. The ROV's attitude sensors allowed an active control of the TX antenna's orientation and tilt, which was less than 5° and 10° of the horizontal for 72 and 96 per cent of all measurements, respectively. For navigational purposes and the determination of distances, the ROV (carrying the TX) and four of the RXs were equipped with a GAPS (IXBLUE) acoustic positioning system. Depending on the signal-to-noise ratio, the accuracy of this system is stated to fall in a range between 0.2 and 1 per cent (@1σ) of the slant range (IXBLUE 2012). With the given slant ranges of 600–700 m during our experiment, this amounts to an accuracy between 1.2 and 7 m (@1σ). This closely matches our observations, in which we found the accuracy of the system to be in the order of 5–8 m. The positions of receivers were also verified by video footage acquired with the ROV. RX4 was not equipped with a transponder and could not, due to shortage of time at the end of the experiment, be found during the last ROV dive. For this station we first used its drop position, which was then corrected by about 37 m to the NW using the approach described by Swidinsky & Edwards (2011).

The station map (Fig. 8) shows the very different style of CSEM experiment with completely arbitrary TX and RX orientations which motivated us to use the previously introduced rotational invariants for the interpretation of the acquired data.

Data example

For processing the measured data sets for each transmission, each containing 15 full cycles (= 1 min) of the transmitted bipolar waveform, were first cut into 15 segments. For each of these segments the measured half-cycles were averaged, which effectively removes the offset. The resulting 15 averaged half-cycles were then log-gated and stacked to yield step-on and step-off responses with corresponding error estimates for each logarithmic time step. We take the standard deviation of the stacking process as standard error of the measured data and use this error in the calculation of error bars for the rotational invariants.

Fig. 11 shows invariants, which were calculated from the processed data at the westerly receiver RX7. For the sake of clarity, we only display TX–RX pairs with distances between 50 and 800 m, since clipping at short distances (∼50 m) and noise at long distances lead to significant distortions of the curves. The remaining 54 TX–RX pairs for this receiver yield invariants, which allow for a first-pass interpretation.

Red and blue lines in Fig. 11 show synthetic responses for homogeneous lower half-spaces of 0.7 and 1.3 Ωm, respectively. The upper section is represented by a 500 m thick, layered conductivity model derived from the CTD data, which is terminated by an infinite air half-space above. Since a finite water depth and the layered conductivity of the water column do have an effect on the invariants at longer offsets, the according synthetic responses are also plotted for the shortest (50 m, dashed) and longest offsets (800 m, solid).

For invariant I_1 (Fig. 11, top left-hand side) it can be seen that all measured invariants fall within the 'corridor' defined by these two synthetic half-space models. We have used this finding to derive an apparent resistivity transformation. In a companion paper by Swidinsky *et al.* (2015) we use this invariant to define an apparent resistivity transformation, which can be used for a fast imaging of CSEM data, which was measured with two separate TX polarizations. For I_4 and even more so for I_2 (Fig. 11, right-hand side) it can
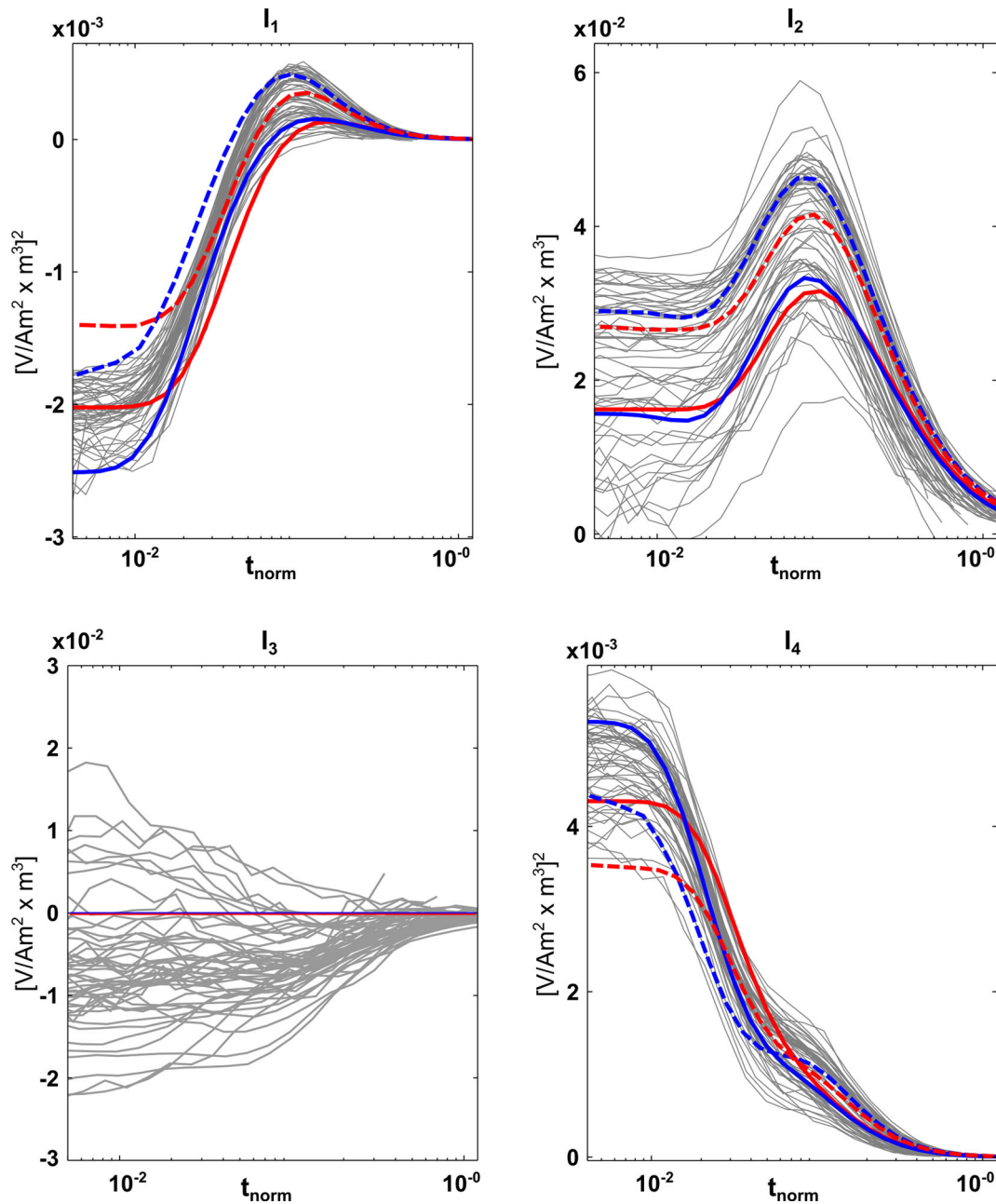
Figure 11. Rotational invariants calculated from real measurements (grey) recorded at receiver 7 on the North Alex Mud Volcano (Fig. 8). Only TX-RX pairs with offsets between 50 and 800 m are displayed. Amplitudes of invariants are scaled by factors of r^3 (I_1 and I_4) or r^6 (I_2 and I_3), where r is the corresponding offset. Times are normalized as in Fig. 4. Additionally, invariants of a 0.7 Ωm (red lines) and a 1.3 Ωm (blue lines) lower half-space are shown for offsets of 50 m (dashed lines) and 800 m (solid lines).

be seen that simple homogeneous half-space models cannot explain the curves. Thus, we will revert to 1-D inversions in the following chapter to investigate if rotational invariants can be explained reasonably well by a layered resistivity model of the subsurface with a significant increase of resistivity at greater depth. For the skew invariant I_3 (Fig. 11, bottom left-hand side) the responses of the half-space models are zero—as shown in the derivation of rotational invariants—but show significant amplitudes for the real data. This could either be an indication for a 3-D resistivity structure, but might also be due to the partially non-planar geometry, bathymetric effects or a bias introduced by errors in the determination of

headings. Ultimately, a 3-D interpretation of the data will be necessary to distinguish possible causes and to fully explain all rotational invariants.

Common midpoint inversion of invariants

Since the experiment was not carried out along extended profiles but rather along many short subprofiles with changing orientations, we constructed a surface grid. For each cell of this grid we simultaneously inverted the data of all TX–RX combinations, whose
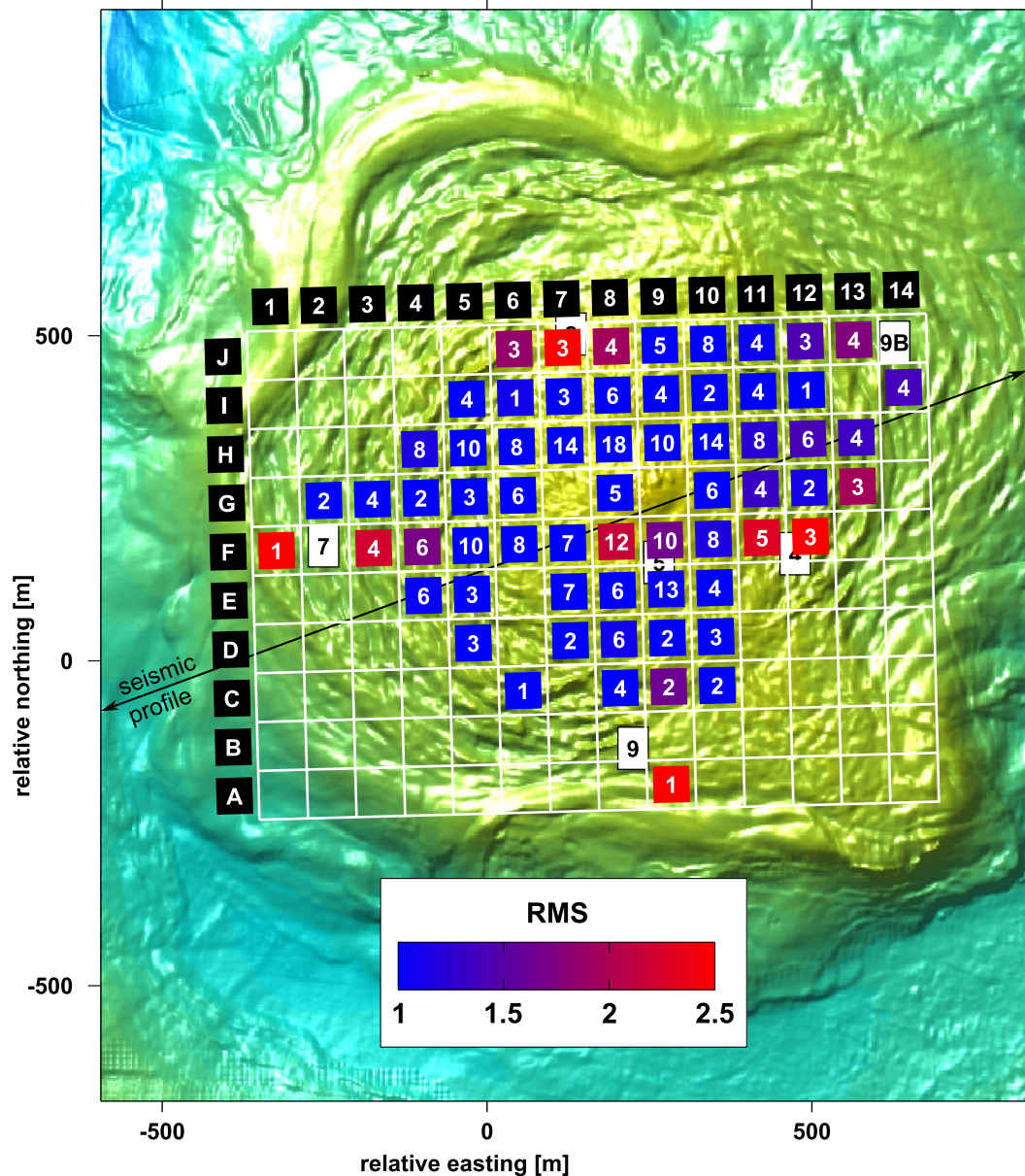
Figure 12. Common midpoint (CMP) grid with 75 m bins with the number of TX–RX combinations whose midpoints fall into the according grid cell indicated inside each cell. The according TX–RX combinations of each CMP cell were simultaneously inverted for in regularized 1D smooth inversions. The colour of cells depict the achieved rms misfit. Labels in black boxes are used to identify CMP cells or profiles in the text. For reference purposes, the locations of receiver stations (white boxes) and of the seismic line are also shown. Map after Feseker *et al.* (2010), changed.

midpoints fall into the respective grid cell, in terms of a 1-D layered model. To achieve a good compromise between lateral resolution and a grid without too many empty cells, we chose a grid spacing of 75 m.

In Sommer *et al.* (2013) we have investigated the effects of the bathymetry for the WND data set. There, we have found that at short TX–RX offsets there can be a significant difference (in terms of the χ^2-misfit) between the transient response of an assumed planar measurement geometry as compared to the response of the true, non-planar measurement geometry (including bathymetry). Especially for TX–RX pairs with offsets of less than 125 m we frequently observed χ^2-misfit above 1. Consequently, we have rejected all offsets of less than 125 m for the CMP inversion. The assumption of a planar geometry also does not hold, if either transmitter or receiver show a significant tilt. This was the case at some locations, where

ridges and troughs formed considerable relief. Therefore, invariants which contain at least one TX polarization with tilt $\geq 10°$ were also rejected. The resulting common midpoint (CMP) coverage for the 75 m bins after rejection of data sets with respect to short offset or excessive tilt is shown in Fig. 12 (white labels).

For the data interpretation we used a constrained regularized 1-D smooth inversion (Constable *et al.* 1987) based on the Matlab function *lsqnonlin*, which is contained in the Optimization Toolbox (Coleman & Li 1994, 1996). For each CMP cell we invert for the resistivities of a multilayered 1-D model. In a 3-D case study, Constable (2010) demonstrated that the marine CSEM method over a 1 Ωm half-space is not sensitive to any structure deeper than or offset by more than about half the source–receiver spacing, which closely matches our experiences. Consequently, for our inversion the depth of the last layer interface is set to 45 per cent of the
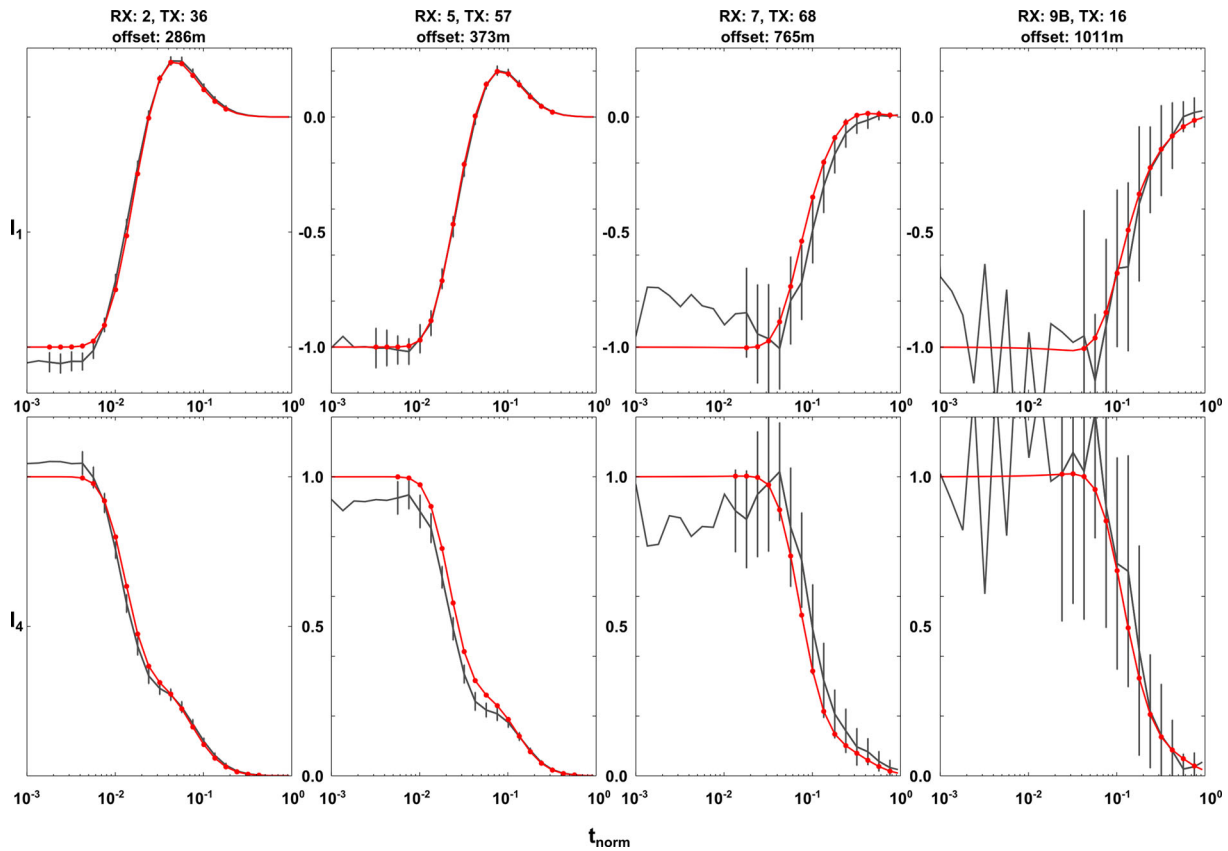
Figure 13. Invariants I_1 and I_4 (top and bottom row, respectively) for four of 14 TX–RX pairs with midpoints falling in CMP grid cell H7. Offsets of the according TX–RX pairs are noted above the plots. Grey lines show invariants calculated from the processed (stacked and log-gated) measurements. For 1-D inversions we used two decades in time ($\rightarrow$ 17 data points in each subplot), which cover the transient part of invariants (note that error bars are only depicted for this transient part of signals). The responses of the best fit model are shown as red lines, the model itself can be found in Fig. 14. For displaying purposes only, amplitudes are normalized to the absolute value of the dc offset and times are normalized as in Fig. 4.

maximum TX–RX offset for each CMP cell. In the same way we determine the first layer interface, which we define at 2 per cent of the minimum TX–RX offset prior to the inversion. Within the inversion we minimize the error normalized rms misfit. Similar to eq. (16), errors for the rotational invariants were derived by error propagation from the errors calculated in the processing of the measured data. Additionally, the positions of TX locations were left as constrained free parameters, which were allowed to vary by at most 5 m in either direction. This was done to account for the accuracy of the GAPS acoustic positioning system. A minimum error floor of 3 per cent of the measured value was assumed to account for errors in the geometry (i.e. distances, tilts, headings; similar in Brown *et al.* 2012) and to avoid a dominant influence of measurements taken at short offsets, which often have very small relative errors.

In the theoretical section we have shown combination of invariants I_1 and I_4 or I_2 and I_4 offer the best parameter resolution (Fig. 7). Since neither invariants, I_1 and I_4, are affected by any potential errors in the heading of receivers, we prefer to use this combination instead of the latter. Within the inversion we use the transient parts of invariants I_1 and I_4.

The distribution of the resulting rms (coloured boxes in Fig. 12) shows that for most CMP cells the misfit has reached a level of around 1, which shows that the chosen combination of invariants are explained within error bounds by the underlying 1-D models. Larger misfits with rms values up to 3 are evident in the direct vicinity of receiver stations. Here, the assumed minimum error

floor of 3 per cent is too small to account for geometrical errors at short offsets.

In Fig. 13 we show a selection of measured step-off transients (grey lines) together with the inversion results (red lines) for the CMP grid cell H7. Subplots are sorted with increasing TX–RX offsets (and thus decreasing signal-to-noise ratios) from left- to right-hand side. This CMP cell was chosen because it is close to the centre of the mud volcano and has a wide spread of TX–RX offsets with good coverage from all directions. The average rms for all 14 stations inverted in this CMP cell is 0.71.

Looking in closer detail at individual curves in Fig. 13 it is evident that while some curves are matched perfectly (e.g. I_1 for RX5–TX57), details of other invariants may not be explained (e.g. I_4 for RX5–TX57). Also, the early parts of the transients, essentially the dc offset, may be underestimated at some stations (e.g. I_1 for RX2–TX36) but overestimated at other stations (e.g. I_4 for RX5–TX57). Here, the 1-D approach is a simplification, which cannot fully explain the transients of TX-RX combinations from different directions, of which the midpoints fall into a common CMP cell. Consequently, a full 3-D interpretation would be necessary to add more degrees of freedom in the underlying resistivity model to further improve the matching of true data and modelled responses. However, since the achieved error levels are quite acceptable and the overall characteristics of the measured transient is matched well in most cases, we are confident that the approach taken does yield a first result, which is meaningful in terms of the true resistivity distribution within the mud volcano.
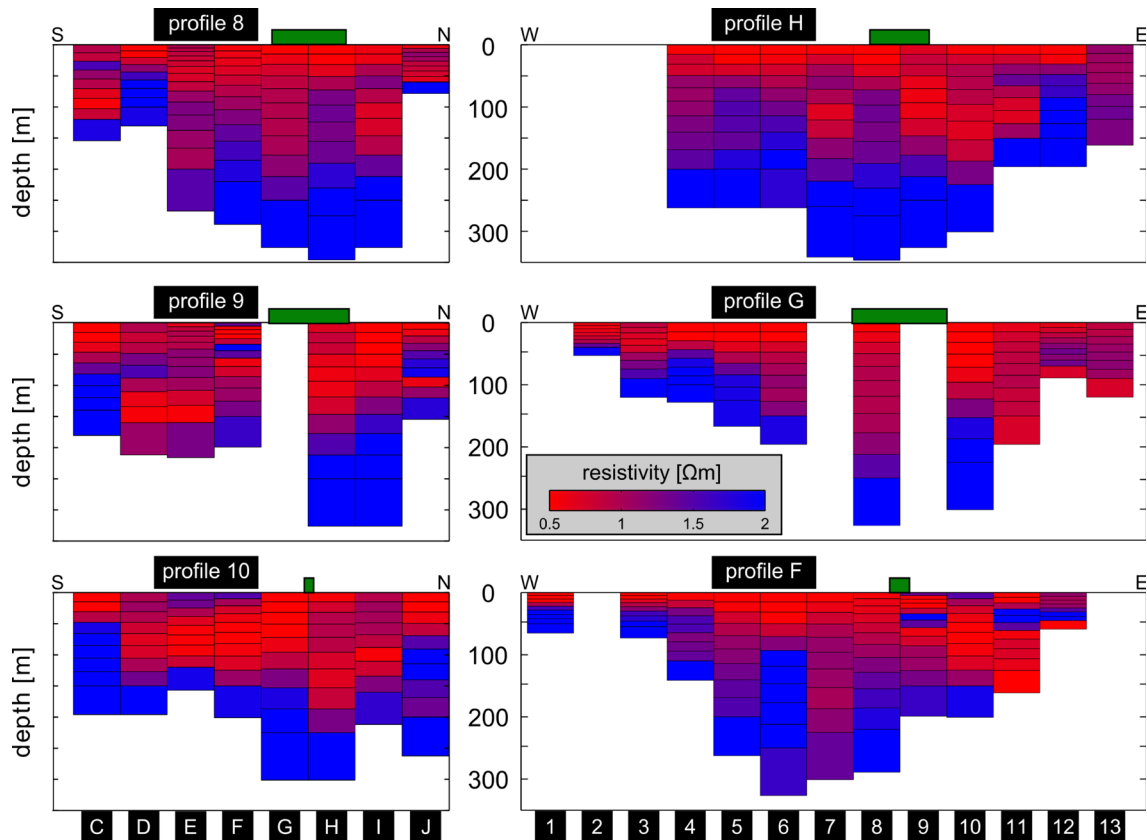
Figure 14. Resistivity sections of CMP inversions in terms of stitched 1-D models. The three S–N (left-hand side) and W–E (right-hand side) striking profiles are the central profiles across the mud volcano. Green boxes above sections depict the central part of the mud volcano, where active venting of gas was observed during the experiment. The maximum model depths vary according to the maximum TX–RX offsets used in the according CMP bins. Note that all plots use the same colourbar and limits. Black labels refer to the location of profiles in Fig. 12.

At shallow depths (≤50 m) the resistivity sections (Fig. 14) are in large parts characterized by low resistivities, for example in the direct centre of the mud volcano (CMP cells G8, H8–9 in Fig. 14), where values in a range between 0.5 and 0.7 Ωm are found. Even though these values are quite low, we will later show that elevated levels of gas saturation are required, which is due to the overall very low resistivity of pore fluids in this part of the mud volcano. Away from the centre, shallow resistive features in the top 100 m, sometimes with resistivities above 1 Ωm, can be found to the S and SE of the centre of the mud volcano (e.g. CMP cells F9–12, E10 and D–E9). These features do not form a smooth structure which we attribute to the changing CMP coverage (Fig. 12) as well as the changing mix of TX–RX offsets at CMP grid cells, which leads to lateral changes of sensitivities on the grid and, thus, contributes to lateral variations in the display of resistivities.

The most prominent feature in the stitched 1-D sections (Fig. 14) can be seen in the increase of resistivity at greater depths, where resistivities frequently reach values between 2.0 and 2.5 Ωm at the maximum penetration depths. In the W–E profiles, the distribution of resistivities shows a general thickening of the more conductive shallow units towards the centre of the mud volcano. For profiles F and H it is hard to interpret this thickening in terms of a continuous layer interface along the profiles. However, along profile G the thickening is systematic and increases from the W towards the centre of the mud volcano (G2–G8) and is then followed by a short upward bend at CMP cell G10. The upward bend is also visible in the easterly stations of profile H (H10–14). The overall picture in the W–E striking CSEM sections indicates a lens-shaped structure

centred beneath the mud volcano, which is similar to the lens-shaped interface visible in the seismic section (Fig. 9).

In Fig. 15 we have combined a line drawing of the seismic section together with models of the CMP inversion along the seismic profile line, which were shifted vertically to match the bathymetry. Furthermore, the depth scale of the CSEM models was adjusted to achieve a structural link between the seismic and the CSEM interpretation. A comparison of the two-way-traveltimes and the depth axis shows that this would require a seismic velocity of $v_p \approx 900$ m s^{-1} in the gas filled sediments above the lens-shaped interface. This value seems reasonable for a hot, gas bearing and unconsolidated sediment. However, it should only be considered as an approximation, since the smooth inversions of the CSEM data set do not yield well-defined layer interfaces but rather smooth transitions, which makes the manual adjustment of layer interfaces from the seismic and CSEM sections subjective to a certain degree.

CSEM models are mostly restricted to the area where incoherent scattering and blanking dominates the seismic section and, thus, results from CSEM are complementary to seismics. A structural link between seismics and CSEM is evident in the westerly part of the mud volcano, where the internal layer from the seismic sections continues into the CSEM models to form the lens-shaped interface. In the easterly part such a structural link is not as obvious, but the general trend of an inclined layer towards the centre of the mud volcano can be seen in both methods. One interesting feature in the CSEM models is the conduit like structure to the SW of the centre of the mud volcano (F7 and G8 in Fig. 15; also E8, not depicted) with low resistivities ($\rho_{bulk} \approx 0.8$–1.2 Ωm) at depths between 150
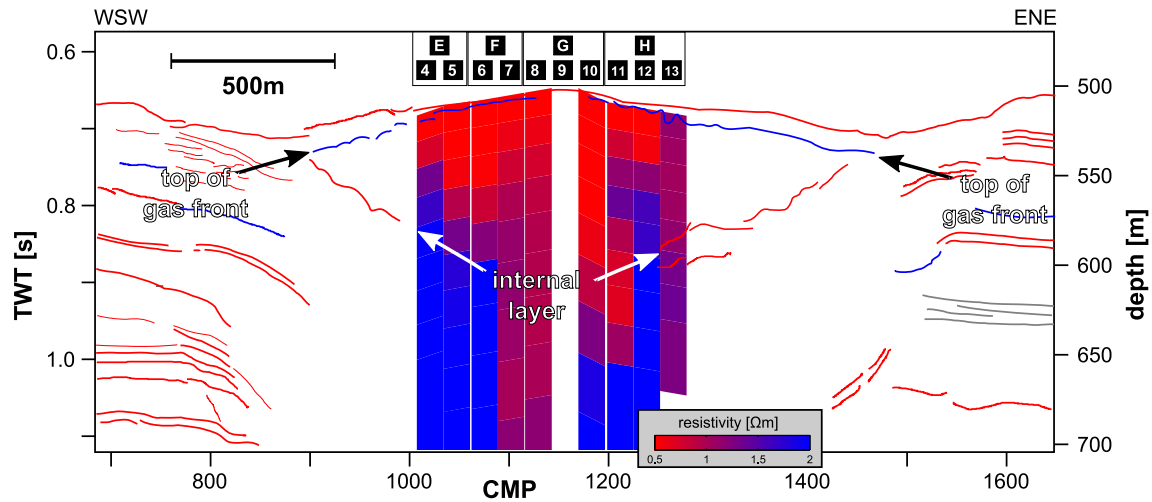
Figure 15. Line drawing from reflections in the seismic section (Fig. 9) with positive, negative and unclear polarity depicted with red, blue and grey lines, respectively. CSEM 1-D models of CMP cells located on the seismic profile line (compare Fig. 8) are displayed in the centre with the CMP cell numbers annotated above the corresponding 1-D models (black labels). The depth scale of the CSEM interpretation (right-hand side) was adjusted to the TWT of seismics by using a velocity of $v_p = 900$ m s^{-1}, which is suitable to achieve a structural match between the sections of the two methods.

and 200 m. This structure is not resolved in the seismic section. The according 1-D models indicate higher resistivities ($\rho_{bulk} \geq 1.5$ Ωm) at depths greater than 225 m, which are not displayed in Fig. 15.

DISCUSSION

We next use the EM inversion results to estimate potential gas saturation levels in the shallow section and to get some further constraints on the nature of resistive feature beneath the lens-shaped interface at depth. This requires a good *a priori* knowledge of the geological setting and geotechnical parameters, as we will show in the following, where we will attempt to interpret the results of the CMP inversions in terms of Archie's Law (Archie 1942):

$$\rho_{bulk} = \rho_f \, \Phi^{-m} \, S_f^{-n}. \tag{19}$$

Here, ρ_{bulk} is the bulk resistivity of sediments, ρ_f is the resistivity of the pore fluid, the formation factor Φ^m combines the porosity Φ and the cementation factor m, S_f is the fluid saturation, and n the saturation exponent.

In a two phase system with gas and a pore fluid, Archie's Law can be used to estimate the gas saturation. In such a system the gas saturation S_g is related to the fluid saturation simply as $S_g = 1 - S_f$ and we can rearrange Archie's Law to:

$$S_g = 1 - \left(\frac{\rho_{bulk}}{\rho_f \cdot \Phi^m} \right)^{1/n}. \tag{20}$$

We will examine the parameters in Archie's Law step by step and use published results and laboratory analyses taken on gravity cores 36, 46 and 100 (see Fig. 8 for location), which were taken during research cruise P362-2 (R/V Poseidon, 2008 February) and later analysed at GEOMAR, to derive plausible parameter ranges:

The first parameter in Archie's Law (19) is the fluid resistivity ρ_f which depends on the concentration of dissolved ions as well as the temperature of the fluid. In the measurement area the resistivity ρ_f of seawater is generally very low with the bottom water reaching a value of about 0.21 Ωm in CTD measurements. In active areas of the mud volcano, seawater in the pore-spaced is replaced by fresher pore fluids from the mud volcano. This can be seen by a sharp drop in chloride concentration at a depth of about 1 m from 600 mmol l^{-1} (= 21.27‰) to 180 mmol l^{-1} (= 6.381‰) in core

100 (Feseker *et al.* 2010) and similar in core 36. The freshening of pore water is explained by expulsion of fluids from within the mud volcano, which are released through dehydration processes of clay minerals at greater depth. The drop in chlorinity can be used to calculate the increase in resistivity of the fresher mud volcano fluids by using the practical salinity scale (Fofonoff 1985) as implemented in the freely available *Seawater Library*: for the chlorinity we first calculate the salinity S to 11.5‰ (salinity = 1.80655 × chlorinity, all in [‰]) and convert to a fluid conductivity of ~1.53 S m^{-1} ($\leftrightarrow \rho_f \approx 0.65$ Ωm) at a temperature of 13.9 °C and a water depth of 500 m using the conductivity ratio R as defined in eq. (1) in Fofonoff (1985).

For a correct characterization of fluid resistivities we also have to take into account the effect of elevated temperatures, which were observed in a confined region with a radius of about 80–100 m around the centre of the mud volcano at the same time of the CSEM experiment. Feseker *et al.* (2010) show several temperature profiles with increases in temperatures from 13.9 °C (bottom seawater) to up to 70 °C, which indicate that steady-state conditions have not been reached at the penetration depth of ~6 m. Thus, temperatures at greater depths possibly reached values in a range between 85 and 100 °C or even higher in the actively venting part of the mud volcano. It is worthwhile to note that only a few years before, maximum temperatures of about 23 °C at a depth of ~12 m were measured during two cruises (Nautinil cruise, R/V L'Atalante, 2003; Mimes cruise, R/V Pelagia, 2004) at the same locations (Feseker *et al.* 2010). Thus, the activity observed in 2008 represented a very recent event, which was observed in a confined region.
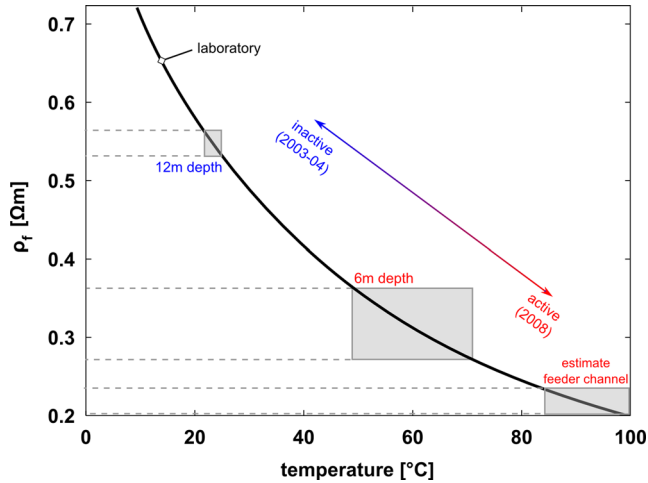
Generally, increased temperatures can be expected to significantly lower the resistivity of the fresher mud volcano fluids. Because the formulas by Fofonoff (1985) are only valid up to temperatures of 30 °C, we use it as a starting point for the temperature—resistivity relationship by Hayashi (2004), which relates fluid resistivity to viscosity:

$$\rho_f(T) = \rho_{f,25} \cdot \left(\frac{\mu_T}{\mu_{25}} \right)^b, \text{ with}$$

$$\log_{10} \left(\frac{\mu_T}{\mu_{25}} \right) = \frac{A(25 - T) - B(25 - T)^2}{t + C}. \tag{21}$$

Here, $\rho_{f,25}$ is the fluid resistivity at 25 °C and constants are given by $A = 1.1278$, $B = 0.001895$ °C^{-1}, $C = 88.93$ °C and $b = 0.877$. The formula is based on a formulation in Sorensen & Glass (1987) in combination with the temperature dependent viscosity of water in Korson *et al.* (1969). It yields reliable values up to 30 °C in Hayashi (2004), and up to 45 °C in Sorensen & Glass (1987). We also tested his formula by comparison to experimental values published by McCleskey (2011) and were able to reproduce conductivities of NaCl solutions of different concentrations (10^{-4}–1 mol kg^{-1}) in a temperature range between 5 and 90 °C with deviations of less than 3.5 per cent. Also, conductivities reported by Quist & Marshall (1968) can be reproduced at a temperature of 105 °C, but are significantly overestimated at a temperature of 205 °C. Thus, we
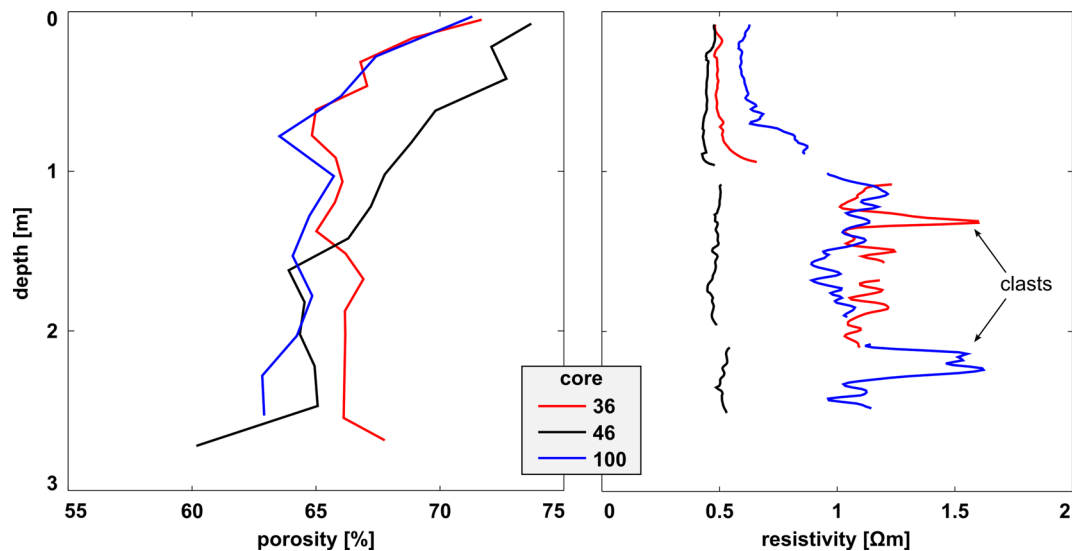
conclude that the formula is suitable to estimate the resistivity of saline pore fluids in a range of temperatures between 0 and 105 °C but should not be used for significantly higher temperatures.

The temperature dependency for the resistivity of the fresher fluids from the mud volcano is shown in Fig. 16. According to our estimates, their resistivity should fall in a range between 0.28 and 0.36 Ωm in areas with measured increased *in situ* temperatures of 50–70 °C (marked area in Fig. 16), but is likely to be even lower within the active feeder channel, where temperatures of around 100 °C seem likely. For these elevated temperatures the resistivity of the mud volcano fluids are estimated to fall in a range between 0.20 and 0.23 Ωm, which would render them practically indistinguishable from regular seawater. At the same time, lower temperatures of about 23 °C, which were observed at the centre of the mud volcano in 2003 and 2004, would yield a significantly higher resistivity of about 0.55 Ωm, which is about a factor 2.5 higher than the one estimated for the active feeder channel.

The second parameters in Archie's Law (19), the formation factor Φ^{-m}, can be derived from measurements on the three gravity cores, which give some constraints on physical parameters in the first ~2.7 m of sediments:

Generally, sediment samples from the mud volcano are mud breccias, which consist of a clay/silt matrix with embedded clasts of various sizes, which are incorporated during the upward transport of mud in the feeder channel (Feseker *et al.* 2010). Porosities (Fig. 17 left-hand side) were calculated after sieving from measurements of the densities of the wet and dried core material. Due to the sieving, porosity measurements only account for the unconsolidated material, while clastic material, which was especially evident in cores from the centre of the mud volcano (cores 36 and 100), is not reflected in the porosities. Porosities in the cores are above 70 per cent directly at the seafloor and drop to values between approximately 63 and 67 per cent below 2 m depth, which we will consider to define the range of porosities for sediments encountered near the mud volcano's surface. Generally, the compaction of undistrubed sediments will lead to a decrease of porosity with depth. Kominz *et al.* (2011) show that for silty sediments the compaction often shows a good to strong exponential reduction of porosity with depth. Using their exponential relationship for marine silts, the porosity range of

Figure 16. Estimated temperature dependency for the resistivity of the mud volcano fluids. which have a depleted chloride concentration of 180 mmol l^{-1} (Feseker *et al.* 2010). Using the practical salinity scale (Fofonoff 1985), this chloride concentration converts to a resistivity of 0.65 Ωm at the temperature of the bottom seawater (13.9 °C), which was extended over a wide temperature range using Hayashi (2004). Grey boxes mark temperature and resistivity ranges during laboratory measurements and different states of activity of the mud volcano.

Figure 17. Porosity data (left-hand side) and resistivity logs (right-hand side) from laboratory measurements on three gravity cores 36, 46 and 100 (for locations refer to Fig. 8). During resistivity logging, core temperatures were around 6 °C for cores 46 and 100 and around 10 °C for core 46. Gaps in the resistivity log occur at the start and end of core sections. Geochemical data of these cores can be found in Feseker *et al.* (2010).
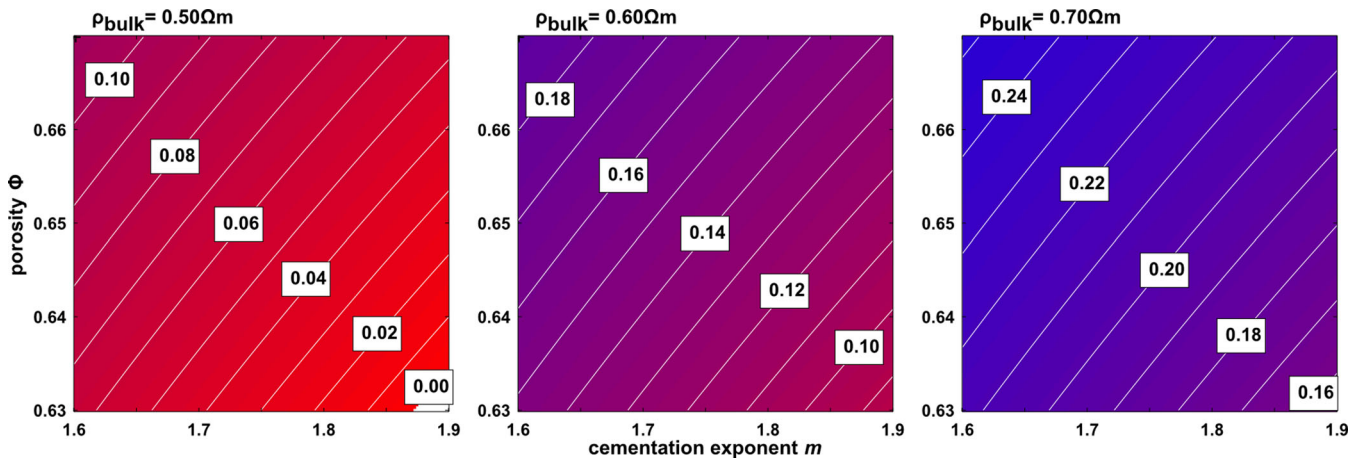
Figure 18. Labelled contour plots of gas saturation S_g at shallow depth for a hot mud volcano fluid ($\rho_f = 0.21$ Ωm). Saturation estimates yield values between 0 and 25 per cent and were calculated using Archie's Law (Archie 1942) with three different bulk resistivities (ρ_{bulk}), which span results from the CMP inversions in the centre of the mud volcano (see Fig. 14).

63–67 per cent near the seafloor would decrease to ranges between 55–58 and 48–51 per cent for depths of 150 and 300 m, respectively, the latter being the maximum depth of penetration in our layered models. Similar estimates would be obtained using their compaction relationship for clay-size clastic sediments, which can also be found in Hamilton (1976). However, it seems likely that—at least in the central part of the mud volcano where material is actively transported towards the surface—porosities of the unconsolidated sediments at greater depth will be higher than estimated by the exponential relationship, possibly reaching values around 60 per cent.

Bulk resistivities were measured with the non-contact-resistivity (NCR) sensor of a multisensor core logger (MSCL, GEOTEK and UK) on split sections of the original water saturated (but most likely degassed) cores (Fig. 17, right-hand side). Resistivities in core 46 show values in a narrow range between 0.44 and 0.53 Ωm, whereas cores 36 and 100 show increasing resistivities below a depth of 1 m. This increase in resistivity is connected to the observed drop in chlorinity, but the generally larger scattering, mostly in the range between 0.85 and 1.25 Ωm with marked peaks of up to 1.7 Ωm, indicates that occurrences of clasts in the core material significantly influence the resistivity at laboratory scale.

The core data (bulk resistivity, fluid resistivity derived from chlorinity and porosity) can be used to calculate the cementation exponent *m* by application of Archie's Law (19). For core 46, which contained only very little clastic material, *m* falls mostly in a range between 1.6 and 1.9. This is in good agreement with the range of 1.4–2 reported for marine sediments by Jackson *et al.* (1978). For cores 36 and 100 values for *m* scatter in a wide range between 0.5 and 4.0. We attribute this to the fact that the porosity data was collected on sieved core samples, whereas measurements of the bulk resistivity were taken on unsieved split cores. Since cores 36 and 100 contained considerable amounts of clastic material, the direct application of Archie's Law to these cores is not feasible. In the following we will consider the range of 1.6–1.9 derived from core 46 to be a suitable range for the cementation exponent *m* and will assume that this range also applies to the central parts of the mud volcano.

The final parameter to be considered in Archie's Law (19) is the saturation exponent *n*. Spangenberg (2001) shows that for marine sediments the saturation index *n* is often similar to the cementation exponent *m*. In agreement with Pearson *et al.* (1983) he suggests an empirical saturation exponent of $n = 1.9386$, which we will use in agreement with our choice of the cementation exponent *m*.

We will first look at bulk resistivities at shallow depths (<50 m) in the centre of the mud volcano (CMP grid cells G8, H8–9 in Fig. 14), which fall in the range between 0.5 and 0.7 Ωm and use eq. (21) for the estimation of gas saturation levels. By confining our example to the centre of the mud volcano we can apply parameters, which are supported by laboratory measurements ($\Phi = 63$–67 per cent, $m = 1.6$–1.9, $n = 1.9386$). and temperature estimates, which are based on in-situ measurements at shallow depth ($\sim$100 °C $\leftrightarrow$ $\rho_f \approx 0.21$ Ωm; Fig. 16). With these parameters, gas saturation are estimated to fall in a range between 0 and 25 per cent (Fig. 18). Under the assumption of lower temperatures (e.g. $\sim$80 °C $\leftrightarrow$ $\rho_f \approx 0.25$ Ωm) gas saturation levels would still fall in a similar range between 0 and 18 per cent. Consequently, an upper bound of $\sim$25 per cent on the level of gas saturation within the shallow central part of the mud volcano can be deduced from the evaluation of the CSEM data. This complements the results of the seismic reflection data, which required some gas saturation to account for the negative impedance contrast at shallow depths, but cannot be used to establish an upper bound on the saturation level.

In the above interpretation, we have not taken into account the effect of clasts, which were found to have a noticeable effect on the bulk resistivity on the laboratory scale (see Fig. 17, right-hand side). It seems possible that clastic material might be concentrated in certain regions of the mud volcano, especially in the centre. Thus, increased resistivities might also be in parts due to such clastic material, which would further lower the required gas saturation. Furthermore, the interpretation of shallow resistivity structure away from the centre of the mud volcano is not advisable at present, because geochemical data and temperature measurements are not available or have not been published, yet.

The interpretation of shallow resistive (≥ 1 Ωm) features in the top 100 m, which can be found to the S and SE of the centre of the mud volcano (CMP cells F9–12, E10 and D–E9 in Fig. 14) is problematic, because the temperature regime was not measured in this part of the mud volcano during the cruises in 2008. We can only state that for a conductive pore fluid with $\rho_f \approx 0.21$ Ωm, gas saturations in the order of 32–45 per cent would be needed to explain the observed bulk resistivities in a range between 1.0 and 1.3 Ωm, which seems unrealistically high. At the same time, a pore fluid with 0.40 Ωm, which could represent a mud volcano fluid at a
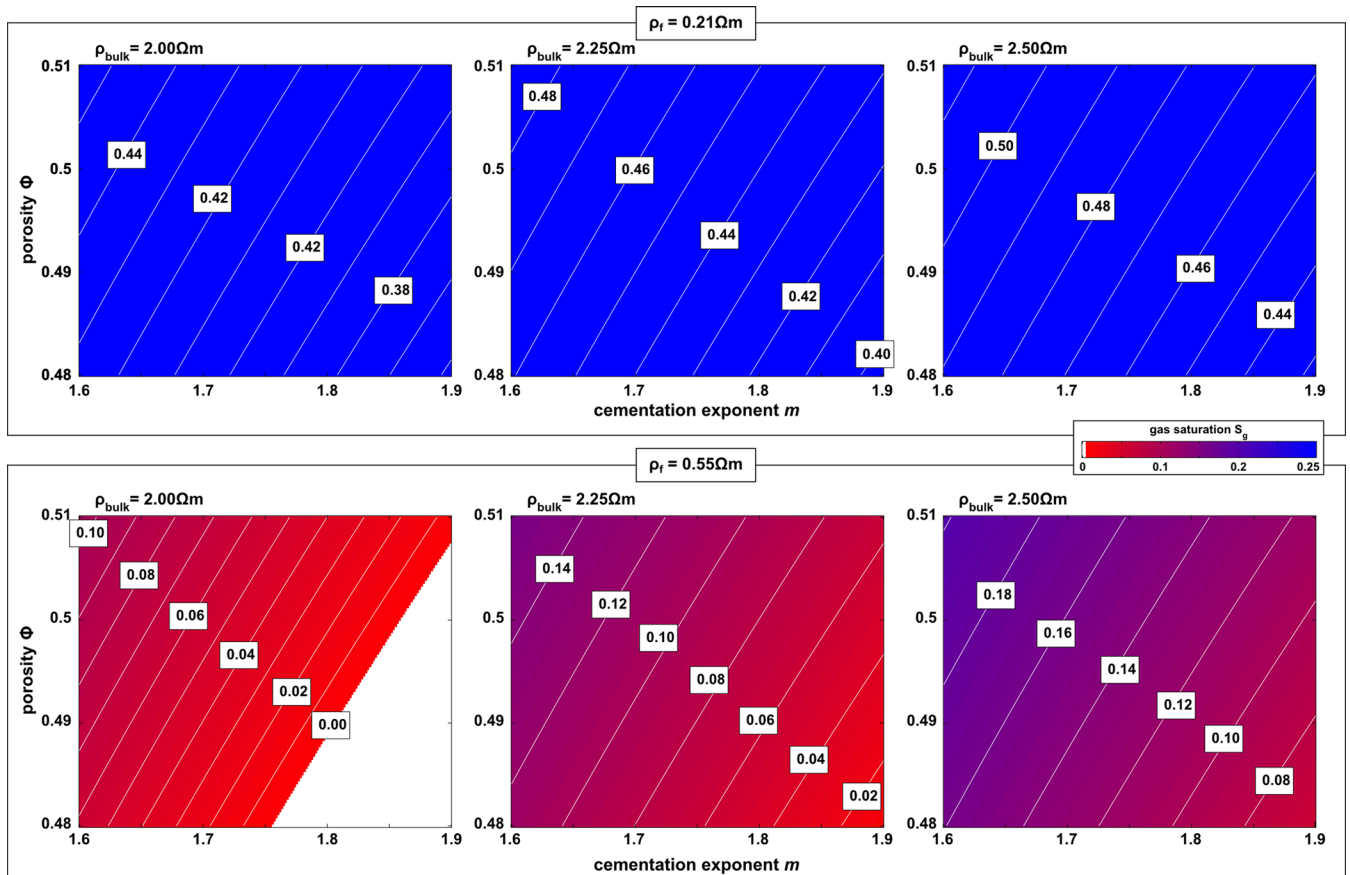
Figure 19. Labelled contour plots of gas saturation S_g at greater depth for a cool mud volcano fluid ($\rho_f = 0.55$ Ωm, top row) and a conductive pore fluid ($\rho_f = 0.21$ Ωm, bottom row). Estimates were calculated using Archie's Law (Archie 1942) with three different bulk resistivities (ρ_{bulk}), which span the majority of results from the CMP inversions (see Fig. 14). Saturation estimates yield values between 36 and 51 per cent (top row) and 0 and 20 per cent (bottom row) for the conductive and resistive pore fluid, respectively. Parameter combinations yielding negative gas saturations have been blanked out.

temperature just above 40 °C, would yield plausible gas saturation levels in a range between 3 and 24 per cent, similar to the estimated range at the centre of the mud volcano. Ultimately, the nature of these shallow resistive features cannot be further constrained with the available data.

To examine possible causes for the increased bulk resistivities, which are encountered beneath the lens-shaped interface, we will use parameter estimates for a depth of 300 m, which were established above ($\Phi = 48$–51 per cent, $m = 1.6$–1.9, $n = 1.9386$). We will argue that for these parameter ranges a pore fluid which is both cool and rather resistive is necessary to explain bulk resistivities in a range between 2.0 and 2.5 Ωm at depth:

For this resistivity range, the assumption of a conductive pore fluid with $\rho_f = 0.21$ Ωm, which could either be seawater or mud volcano fluids at high temperatures of ~100 °C, would require exceptionally high gas saturations between 36 and 51 per cent (Fig. 19, top panel). Even a lowering of the porosity to 35 per cent to account for unrealistically high compaction of sediments at a collapsed surface of an old mud volcano generation would still require gas saturations well above 10 per cent for conductive pore fluids. However, gas saturations above 10 per cent would be in conflict with the positive impedance contrast observed in the seismic section. Thus, it seems not plausible that conductive pore fluids are widespread at greater depth beneath the lens-shaped interface, at least not in combination with unconsolidated sediments as found at the present mud volcano surface. The preclusion of a widespread occurrence of conductive

fluids also precludes that high temperatures prevail throughout the whole structure of the mud volcano at these depths. Furthermore, the assumption of a large temperature anomaly at depth would also contradict the fact that the observed high activity in 2008 must have been a recent event, since the mud volcano was found in a dormant stage during two cruises in 2003 and 2004. However, conductive fluids and high temperatures could exist in a confined region like the feeder channel, which might be indicated as conduit like structure at a depth of 150–200 m to the SSW of the centre of the mud volcano in the resistivity section.

The assumption of a resistive pore fluid with $\rho_f = 0.55$ Ωm (Fig. 19, bottom panel), which would represent cooled down mud volcano fluids, can explain bulk resistivities in a range between 2.0 and 2.5 Ωm, if gas saturation levels are between 0 and 20 per cent. Saturation levels well below 10 per cent, which are required for the positive impedance contrast in the seismic image, can be obtained if porosities are assumed in the lower range ($\Phi \leq 49$ per cent) and cementation exponents in the upper range ($m \geq 1.8$). This would be in agreement with the interpretation that we see a lithological change across the lens-shaped interface, in which the surface of an older generation of the mud volcano separates older, more compacted and cemented mud volcano sediments from fresh sediments, as suggested by Perez-Garcia *et al.* (2009) for the Håkan Mosby mud volcano. Also, the existence of large amounts of cooler mud volcano fluids at depth would be in agreement with both the seismic and the CSEM results.

Consequently, the best explanation for increased resistivities between 2.0 and 2.5 Ωm at depth, at least in terms of Archie's law, is a lithological change to a sequence with lower porosity and higher cementation, possibly in connection to a pore fluid, which is more resistive than either seawater or a hot mud volcano fluid. The lithological change could either be interpreted in terms of a higher compaction of mud volcano sediments or could also relate to higher abundances of carbonates at an old mud volcano surface, since clastic material transported from greater depth is seen to have a noticeable effect on the bulk resistivity at laboratory scale (see Fig. 17, right-hand panel).

Any gas present should only be existent at saturations levels well below 10 per cent. Ultimately, a 3-D interpretation of the CSEM data is necessary to decide, if this is a true structural feature or rather a footprint of the acquisition geometry in combination with the 1-D interpretations.

Generally, better constraints on the geotechnical parameters from additional bore holes, which are however not available at the moment, and a sophisticated geothermal modelling would be required to further improve the significance of the CSEM interpretation. Also, it is clear that a true 3-D interpretation of the CSEM data will be needed to better account for the topography of the mud volcano and the varying transmitter–receiver geometries, which sometimes significantly deviate from the assumption of a planar geometry. However, since we have restricted our interpretation to general features in the CSEM sections and see a good structural agreement at depth between the CSEM and the seismic sections, we are confident that our interpretations are meaningful in terms of the geology of the mud volcano and do not simply reflect an acquisition footprint of the experiment.

CONCLUSION

A novel marine CSEM experiment was conducted at the North Alex mud volcano located in the West Nile Delta. It employed a transmitter, which was mounted on an ROV. This allowed for a real placement of the transmitter in two nearly perpendicular polarizations at each transmitter location.

The data set was analysed using the concept of rotational invariants, adapted from the land-based case to the marine case. The sensitivity of combinations of invariants to the resistivity structure of the underground is superior to responses, which relate only to a single transmitter polarization. As additional benefit, two of the derived rotational invariants (I_1 and I_4) are independent of the receiver orientation, permitting the interpretation of data without bias by directional uncertainties of receivers.

The CMP inversion of rotational invariants results in 1-D resistivity sections, which show a structural link to results from reflection seismics: both methods see a lens-shaped interface, which could extend down to a depth of about 150 m. The interface is interpreted as an old surface of the mud volcano, since observed bulk resistivities in a range between 2.0 and 2.5 Ωm below the lens-shaped interface require a combination of higher compaction and increased cementation. Also, increased resistivities are indicative for a pore fluid with increased resistivity at depth. This interpretation is in accordance to Perez-Garcia *et al.* (2009), who describe a similar structure at the Håkon Mosby mud volcano.

No obvious resistive structure is evident at shallow depths in the centre of the mud volcano, although a shallow reflector with inverted polarity is visible in the seismic section and substantial activity with degassing and fresh pore fluids were observed in this region. This unexpected result is due to the high temperatures in the central part of the mud volcano, which substantially lower the resistivity of the fresh mud volcano fluid to a point, where it becomes similar to that of seawater ($\rho_f \approx 0.21$ Ωm). For the central part of the mud volcano the characteristics of the pore fluid (i.e. salinity and temperature) as well as the geotechnical parameters are sufficiently well known, and gas saturation levels are estimated to falls in a range between 0 and 25 per cent for observed bulk resistivities between 0.5 and 0.7 Ωm. Consequently, high temperatures in the central part of the mud volcano lower bulk resistivities and, thus, mask the presence of potentially significant amounts of gas in the resistivity section. Nevertheless, the estimated saturation levels are a quantitative measure, which could not be deduced from apparent resistivities in Swidinsky *et al.* (2015). Furthermore, they complement the information from reflection seismics, which is indicative for the existence of gas but not suitable to determine an upper bound on the saturation level.

The missing geological interpretation of resistivity sections for the off-centre regions of the mud volcano require the addition of temperature measurements & geochemical analyses to the, which have been measured but are yet unpublished. The current data set is suitable for a full 3-D interpretation, which is work in progress. This interpretation can be guided by analysis of the skew invariant I_3, which is sensitive to the dimensionality of the underlying resistivity structure.

REFERENCES

Anderson, C. & Mattson, J., 2010. An integrated approach to marine electromagnetic surveying using a towed streamer and source, *First Break,* **28,** 71–75.

Archie, G., 1942. The electrical resistivity log as an aid in determining some reservoir characteristics, *Petrol. Trans. AIME,* **146,** 54–56.

Bibby, H., 1977. The apparent resistivity tensor, *Geophysics,* **42,** 1258–1261.

Bibby, H., 1986. Analysis of multiple-source bipole-quadrupole resistivity surveys using the apparent resistivity tensor, *Geophysics,* **51,** 972–983.

Brown, V., Hoversten, M., Key, K. & Chen, J., 2012. Resolution of reservoir scale electrical anisotropy from marine CSEM data, *Geophysics,* **77,** E147–E158.

Cairns, G., Evans, R. & Edwards, R.N., 1996. A time domain electromagnetic survey of the TAG hydrothermal mound, *Geophys. Res. Lett.,* **23,** 3455–3458.

Caldwell, T. & Bibby, H., 1998. The instantaneous apparent resistivity tensor: a visualization scheme for LOTEM electric field measurements, *Geophys. J. Int.,* **135,** 817–834.

Coleman, T. & Li, Y., 1994. On the convergence of reflective newton methods for large-scale nonlinear minimization subject to bounds, *Math. Program.,* **67,** 189–224.

Coleman, T. & Li, Y., 1996. An interior trust region approach for nonlinear minimization subject to bounds, *SIAM J. Opt.,* **6,** 418–445.

Constable, S., 2010. Ten years of marine CSEM for hydrocarbon exploration, *Geophysics,* **75**(5), 75A67–75A81.

Constable, S. & Cox, C., 1996. Marine controlled-source electromagnetic sounding, 2, The PEGASUS experiment, *J. geophys. Res.,* **101,** 5519–5530.

Constable, S., Parker, R. & Constable, C., 1987. Occam's inversion: a practical algorithm for generating smooth models from electromagnetic sounding data, *Geophysics,* **52,** 289–300.

Dupre, S. *et al.*, 2007. Seafloor geological studies above active gas chimneys off Egypt (Central Nile deep sea fan), *Deep-Sea Res. Part I – Oceanogr. Res. Papers,* **54,** 1146–1172.

Edwards, R.N., 1997. On the resource evaluation of marine gas hydrate deposits using a sea-floor transient electric dipole-dipole methods, *Geophysics,* **62,** 63–74.

Edwards, R.N. & Chave, A.D., 1986. A transient electric dipole-dipole method for mapping the conductivity of the sea-floor, *Geophysics,* **51,** 984–987.

Feseker, T., Dählmann, A., Foucher, J.P. & Harmegnies, F., 2009. In-situ sediment temperature measurements and geochemical pore water data suggest highly dynamic fluid flow at Isis mud volcano, eastern Mediterranean Sea, *Mar. Geol.,* **261,** 128–137.

Feseker, T., Brown, K., Blanchet, C., Scholz, F., Nusso, M., Reitz, A., Schmidt, M. & Hensen, C., 2010. Active mud volcanos on the upper slope of the western Nile deep-sea fan—first results from the P362/2 cruise of R/V Poseidon, *Geo-Mar. Lett.,* **30,** 169–186.

Fofonoff, N., 1985. Physical properties of seawater: a new salinity scale and equation of state for seawater, *J. geophys. Res.,* **90,** 3332–3342.

Hamilton, E., 1976. Variations of density and porosity with depth in deep-sea sediments, *J. Sediment. Petrol.,* **46,** 280–300.

Hayashi, M., 2004. Temperature-electrical conductivity relation of water for environmental monitoring and geophysical data inversion, *Environ. Monitor. Assess.,* **96,** 119–128.

Hensen, C., Nuzzo, M., Hornibrook, E., Pinheiro, L.M., Bock, B., Magalhaes, V.H. & Brückmann, W., 2007. Sources of mud volcano fluids in the Gulf of Cadiz—indications for hydrothermal imprint, *Geochim. Cosmochim. Acta,* **71,** 1232–1248.

IXBLUE, 2012. *GAPS – Carbon V.1 – User Guide,* Manual, 148 pp.

Jackson, P., Smith, D.T. & Stanford, P., 1978. Resistivity-porosity-particle shape relationships for marine sands, *Geophysics,* **43,** 1250–1268.

Kominz, M., Patterson, K. & Odette, D., 2011. Lithology dependence of porosity in slope and deep marine sediments, *J. Sediment. Res.,* **81,** 730–742.

Kopf, A., 2002. Significance of mud volcanism, *Rev. Geophys.,* **40,** 1–52.

Korson, L., Drost-Hansen, W. & Millero, F., 1969. Viscosity of water at various temperatures, *J. Phys. Chem.,* **73,** 34–39.

Li, X. & Pedersen, L., 1994. Comment on 'Three dimensional interpretation of multiple-source bipole-dipole resistivity data using the apparent resistivity tensor' by Bibby, H.M. & Hohmann, G.W., *Geophys. Prospect.,* **42,** 525–526.

McCleskey, R., 2011. Electrical conductivity of electrolytes found in natural waters from 5–90 °C, *J. Chem. Eng. Data,* **56,** 317–327.

Minshull, T.A., Singh, S.C. & Westbrook, G.K., 2012. Seismic velocity structure at a gas hydrate reflector, offshore western Colombia, from full waveform inversion, *J. geophys. Res.,* **99**(B3), 4715–4734.

Munkholm, M. & Auken, E., 1996. Electromagnetic noise contamination on transient electromagnetic soundings in culturally disturbed environments, *J. Environ. Eng. Geophys.,* **1,** 119–127.

Newman, G., Commer, M. & Carazzone, J., 2010. Imaging CSEM data in the presence of electrical anisotropy, *Geophysics,* **75**(2), F51–F61.

Pearson, C., Halleck, P., McGire, P., Hermers, R. & Mathews, M., 1983. Natural gas hydrate deposits: a review of *in situ* properties, *J. Phys. Chem.,* **87,** 4180–4185.

Perez-Garcia, C., Feseker, T., Mienert, J. & Berndt, C., 2009. The Håkon Mosby mud volcano: 330000 years of focused fluid flow activity at the SW Barents Sea slope, *Mar. Geol.,* **262,** 105–115.

Quist, A. & Marshall, W., 1968. Electrical conductances of aqueous sodium chloride solutions from 0 to 800° and at pressures to 4000 bars, *J. Phys. Chem.,* **72,** 684–703.

Risk, G.F., Bibby, H.M. & Caldwell, T.G., 1993. DC resistivity mapping with the multiple-source bipole-dipole array in the central volcanic region, New-Zealand, *J. Geomagn. Geoelectr.,* **45,** 897–916.

Scholl, C. & Edwards, R.N., 2007. Marine downhole to seafloor dipole-dipole electromagnetic methods and the resolution of resistive targets, *Geophysics,* **72,** WA39–WA49.

Schwalenberg, K., Häckel, M., Poort, J. & Jegen, M., 2010. Evaluation of gas hydrate deposits in an active seep area using marine controlled source electromagnetics: Results from Opouawe Bank, Hikurangi Margin, New Zealand, *Mar. Geol.,* **272,** 79–88.

Sommer, M., Hölz, S., Moorkamp, M., Swidinsky, A., Heincke, B., Scholl, C. & Jegen, M., 2013. GPU parallelization of a three dimensional marine CSEM code, *Comput. Geosci.,* **58,** 91–99.

Sorensen, J. & Glass, G., 1987. Ion and temperature dependence of electrical conductance for natural waters, *Anal. Chem.,* **59,** 1594–1597.

Spangenberg, E., 2001. Modeling of the influence of gas hydrate content on the electrical properties of porous sediments, *J. geophys. Res.,* **106,** 6535–6548.

Stolt, R., 1978. Migration by Fourier transform, *Geophysics,* **43,** 23–48.

Swidinsky, A. & Edwards, R.N., 2011. Joint inversion of navigation and resistivity using a fixed transmitter and a towed receiver array: a transient marine CSEM model study, *Geophys. J. Int.,* **186,** 987–996.

Swidinsky, A., Hölz, H. & Jegen, M., 2012. On mapping seafloor mineral deposits with central loop transient electromagnetics, *Geophysics,* **77,** E171–E184.

Swidinsky, A., Hölz, S. & Jegen, M., 2015. Rapid resistivity imaging for marine CSEM surveys with two transmitter polarizations: an application to the North Alex mud volcano, *Geophysics,* **80**, doi:10.1190/GEO2014-0015.1.

Weitemeyer, K. & Constable, S., 2010. Mapping shallow geology and gas hydrate with marine CSEM surveys, *First Break,* **28,** 97–102.